Journal of Computational Physics **181,** 68–97 (2002)
doi:10.1006/jcph.2002.7119

Large Eddy Simulation of High-Reynolds-Number Free and Wall-Bounded Flows

Christer Fureby* and Fernando F. Grinstein†

*Weapons and Protection Division, Warheads and Propulsion, The Swedish Defense Research Agency, FOI, S-172 90, Stockholm, Sweden; and †Laboratory for Computational Physics & Fluid Dynamics, Code 6410, Naval Research Laboratory, Washington, DC 20375-5344
E-mail: grinstei@lcp.nrl.navy.mil

Received January 23, 2001; revised November 5, 2001

The ability to simulate complex unsteady flows is limited by the current state of the art of subgrid-scale (SGS) modeling, which invariably relies on the use of Smagorinsky-type isotropic eddy-viscosity models. Turbulent flows of practical importance involve inherently three-dimensional unsteady features, often subjected to strong inhomogeneous effects and rapid deformation, which cannot be captured by isotropic models. Although some available improved SGS models can outperform the isotropic eddy-viscosity models, their practical use is typically limited because of their complexity. Development of more-sophisticated SGS models is actively pursued, and it is desirable to also investigate alternative nonconventional approaches. In ordinary large eddy simulation (LES) approaches models are introduced for closure of the low-pass filtered Navier–Stokes equations (NSE). A promising LES approach is the monotonically integrated LES (MILES), which involves solving the unfiltered NSE using high-resolution monotone algorithms; in this approach, implicit SGS models, provided by intrinsic nonlinear high-frequency filters built into the convection discretization, are coupled naturally to the resolvable scales of the flow. Formal properties of the effective SGS modeling using MILES are documented using databases of simulated free and wall-bounded inhomogeneous flows, including isotropic decaying turbulence, transitional jets, and channel flows. Mathematical and physical aspects of (implicit) SGS modeling through the use of nonlinear flux limiters are addressed using a formalism based on the modified LES equations.

1. INTRODUCTION

The Navier–Stokes equations (NSE), supplemented by empirical laws for the dependence of viscosity and thermal conductivity with other flow variables and by a constitutive law defining how the pressure depends on the other flow variables, can be used to describe all flow phenomena in a linear viscous fluid. In addition, appropriate initial and boundary

0021-9991/02 $35.00

conditions must be supplied to ensure the well-posedness of the NSE and to select the specific physical flow realizations to be emulated. From a computational point of view, the NSE can be solved directly for laminar flows, while for turbulent flows the wide range of eddy scales to be captured prohibits direct numerical simulation (DNS). The prevalent remedy to this resolution problem involves the Reynolds-averaged Navier–Stokes (RANS) equations, i.e., the averaged NSE, with averaging typically carried out over time, over homogeneous directions, or across an ensemble of equivalent flows, which additionally requires empirical or (at least) semiempirical information on the turbulence structure and its relation to the mean flow. A more viable approach is the large eddy simulation (LES) method, whereby only the small-scale turbulent fluctuations are modeled and the larger scale fluctuations are computed directly (see, e.g., [1], and references therein).

The technique of LES has emerged as a hopeful alternative to the RANS approach in order to confront the scale-complexity problem inherent to high Re-number turbulent flows [2]. In LES, the motion is separated into small and large scale and equations are solved for the latter. The separation is achieved by means of a low-pass filter, which can be formulated in several ways, such as by use of an integral filter or by projection onto a finite set of basis functions. In LES, the filter is usually applied by convolving all dependent variables with a predefined filter kernel $G(\mathbf{x}, \Delta)$ to extract the large-scale components. Accordingly, the filtering is devised to eliminate eddies smaller than the filter width Δ. Convolving the NSE with G under the assumption that filtering and differentiation commute [3, 4] results in equations for the large-scale resolvable components, often referred to as the grid-scale (GS) components. The LES equations also contain unresolved transport terms, i.e., subgrid-scale (SGS) terms representing effects of the SGS flow on the resolved GS flow [1, 5, 6]. Prior to discretization, the SGS terms must be modeled using information from the resolved flow at a spatial resolution near Δ, which is typically more affordable than DNS—requiring a resolution near the Kolmogorov scale $\lambda_K \ll \Delta$. In the absence of an accepted universal theory of turbulence to solve the problem of SGS modeling, the development and improvement of such models must include the rational use of empirical information. Present-day SGS models include algebraic, one-equation eddy-viscosity, scale similarity, and differential stress models, of which the former can be of both a static and a dynamic nature, as well as SGS models developed in some adjoint space, such as the renormalization group, structure function, and eddy-damped quasinormal Markovian models (e.g., [1, 5, 6]). Although some of these models can outperform the isotropic eddy-viscosity models, their practical use is typically limited by their complexity, and it is thus desirable to also investigate alternative nonconventional approaches.

Far from walls the SGS flow is ideally considered homogeneous isotropic. However, laboratory studies [7] and numerical simulations [8] proved the existence of highly organized vortical structures—with concentrations of vorticity in elongated filaments or "worm" vortices characterizing the smallest coherent structures (CS) of turbulent flows [9–11]. The typical cross-sectional diameter of the worm vortices in isotropic homogeneous turbulent flows is $4\lambda_K$–$10\lambda_K$, while the radius of intense elongated vortices in the near-wall region of turbulent wall-bounded flows scales in viscous units [12]. The existence of worm vortices can be traced to an inherently anisotropic feature of the small-scale organization of turbulent flows: the fact that high-magnitude vorticity is preferentially aligned with the eigenvector corresponding to the intermediate eigenvalue of the rate-of-strain tensor with very little such preferential alignment for the lower magnitude vorticity [13, 14]. This is a kinematic property independent of the dynamics involved in the vorticity generation [9, 12], and it

suggests that characteristic small-scale CS in turbulent flows can be locally regarded as two-dimensional structures stretched by strain that is weaker than the small-scale vorticity—a concept that has been used when developing vortex-based SGS models [15, 16].

Turbulent flows near walls are characterized by much-less-universal properties. Close to the wall the length scales of the most energetic eddies decrease, and if the computational grid in a LES is unable to resolve these length scales then anisotropy in the turbulent flow will become anisotropy of the SGS motion, thus necessitating SGS models capable of handling simultaneous flow and grid anisotropy. LES of wall-bounded flows are believed to be limited to Re numbers that are just a factor of two larger than those achievable with DNS [17], and fine grids are believed to be necessary to resolve the mechanisms responsible for self-sustaining turbulence in wall flows [18].

Moreover, turbulent flows of practical importance involve inherently three-dimensional unsteady features, often subjected to strong mean inhomogeneous effects and rapid deformation playing an important role in determining the Reynolds stresses. It has been shown that in the case of inhomogeneous flows—where the filtering operation is necessarily performed in physical space—the SGS terms contain two components: a rapid part that is explicitly dependent on the mean velocity gradient, and a slow part that is not [19]. The rapid part cannot be captured by eddy-viscosity models and plays a significant role when the turbulence is in a nonequilibrium state with production much larger than dissipation, or when the filter size is not very small compared to the integral scale of the turbulence, as is typically the case in practical LES applications.

In seeking an alternative LES model formulation, we choose here to recognize two crucial aspects of turbulent flows to be captured: (i) the dominant vortex interaction mechanisms underlying the cascade dynamics in the inertial subrange occur on convective time scales much shorter than the diffusive time scales and are thus essentially inviscid; (ii) when the worm vortices are thinner than the main flow scales details of their internal structure (and core diameters) may no longer be significant, and the strengths and positions of the cores of such characteristic regions of intense vorticity may be the most important features to be simulated. We are thus led to considering the concept of LES based on sharp velocity-gradient capturing schemes. Promising LES approaches focusing on these aspects are based on solving the NSE or Euler equations using high-resolution schemes such as the flux-corrected transport (FCT) method [20], or the piecewise parabolic method (PPM) [21]. In this monotonically integrated LES (MILES) [22, 23], nonlinear high-frequency filters built into the algorithms provide implicit SGS models—in contrast to conventional LES, where explicit SGS models are introduced for closure prior to discretization.

An important numerical consideration when evaluating LES schemes is the need to use an analysis framework, which will readily exhibit interactions between explicit SGS terms and leading-order truncation errors—which often are of the same order of magnitude, irrespective of whether finite difference, finite volume, or finite element discretization are utilized. The modified LES equations provide such a framework. In the absence of an explicit SGS model, the modified LES equations analysis can likewise be used to address the extent to which leading-order truncation errors can provide an implicit SGS model when suitable algorithms are used. In the present study, this framework of analysis is used to address the formal aspects of effective SGS modeling with MILES.

The plan of the paper is as follows. An overview of the conventional LES approach is presented in Section 2, followed by its numerical analysis in Section 3, which is then used as reference for the formal discussion of MILES presented in Section 4. Properties of

SGS modeling using MILES are documented in Section 5, using the database of simulated free and wall-bounded flows; the approach is tested in a broad range of representative applications, including homogeneous isotropic decaying turbulence, transitional jets, and channel flows.

2. THE CONVENTIONAL LES APPROACH

The fluid dynamical model used is based on the NSE [24]. In ordinary LES all variables f are split into GS and SGS components, $f = \bar{f} + f'$, where $\bar{f} = G * f$ is the GS component, $G = G(\mathbf{x}, \Delta)$ is the filter function, and $\Delta = \Delta(\mathbf{x})$ is the filter width. For variable density flows, Favre filtering $\tilde{f} = \overline{\rho f}/\bar{\rho}$ is employed so that $f = \tilde{f} + f''$. The LES equations result from convolving the NSE with G, viz.,

$$\begin{cases} \partial_t(\bar{\rho}) + \nabla \cdot (\bar{\rho}\,\tilde{\mathbf{v}}) = m^{\rho}, \\ \partial_t(\bar{\rho}\,\tilde{\mathbf{v}}) + \nabla \cdot (\bar{\rho}\,\tilde{\mathbf{v}} \otimes \tilde{\mathbf{v}}) = -\nabla \bar{p} + \nabla \cdot (\bar{\mathbf{S}} - \mathbf{B}) + \bar{\rho}\,\tilde{\mathbf{f}} + \mathbf{m}^{v}, \\ \partial_t(\bar{\rho}\,\tilde{e}) + \nabla \cdot (\bar{\rho}\,\tilde{\mathbf{v}}\tilde{e}) = \nabla \cdot (\bar{\mathbf{h}} - \mathbf{b}) + \bar{\mathbf{S}} \cdot \tilde{\mathbf{D}} + \bar{\rho}\varepsilon + \bar{\rho}\tilde{\sigma} + m^{e}, \end{cases} \tag{1}$$

where ρ is the density, $\mathbf{v}$ the velocity, p the pressure, $\mathbf{S} = (\lambda + \frac{2}{3}\mu)\mathrm{tr}\mathbf{D}\mathbf{I} + 2\mu\mathbf{D}_{\mathrm{D}}$ the viscous stress tensor, $\mathbf{f}$ the specific body force field, $\mathbf{B} = \bar{\rho}(\widetilde{\mathbf{v} \otimes \mathbf{v}} - \tilde{\mathbf{v}} \otimes \tilde{\mathbf{v}})$ the SGS stress tensor, $e = \int_{T_0}^{T} c_V\, dT$ the internal energy (with T the temperature and c_V the specific heat at constant volume), $\mathbf{h} = \kappa \nabla T$ the heat flux vector, $\mathbf{b} = \bar{\rho}(\widetilde{\mathbf{v}e} - \tilde{\mathbf{v}}\tilde{e})$ the SGS flux vector, $\bar{\rho}\varepsilon = \overline{\mathbf{S} \cdot \mathbf{D}} - \bar{\mathbf{S}} \cdot \tilde{\mathbf{D}}$ the SGS dissipation, and σ the nonmechanical netpower. λ and μ are the molecular viscosities, κ the thermal conductivity, $\mathbf{D} = \frac{1}{2}(\mathbf{L} + \mathbf{L}^{T})$ the rate-of-strain tensor, and $\mathbf{L} = \nabla \mathbf{v}$ the velocity gradient. Furthermore, the terms m^{ρ}, $\mathbf{m}^{v}$, and m^{e} are the results of the noncommuting filter, $[\nabla, G*]f = (\frac{\partial G}{\partial \Delta} * f)\nabla\Delta + (Gf\mathbf{n})_{\partial \mathrm{D}}$. Fureby and Tabor [4] analyzed these terms and found them to be nonzero only in the wall proximity and in regions with grid stretching. These terms can be either neglected, as is commonly done, or included in the unresolved transport terms $\nabla \cdot \mathbf{B}$ and $\nabla \cdot \mathbf{b}$ in the LES equations (1).

Models for $\mathbf{B}$, $\mathbf{b}$, and ε are required to close the LES equations (1) and to emulate the effects of the SGS flow physics on the GS flow. The SGS stress tensor and flux vector can be partitioned into Leonard, cross, and Reynolds terms representing interactions between GS eddies, between GS and SGS eddies, and between SGS eddies, respectively. Mathematical analysis and physical arguments [4, 25, 26] suggest that $\mathbf{B}$ is a Grammian tensor provided that $G = G(|\mathbf{x}|, \Delta)$, which further implies that $\mathbf{B} \in Psym$, where $Psym$ is the set of all positive definite symmetric tensors. By requiring that the LES equations (1) should have the same transformation properties as the NSE under a change of frame it is evident [4, 25] that $\mathbf{B}$ and $\mathbf{b}$ are frame indifferent and hence isotropic functions [27] in their arguments $\bar{\rho}$, $\tilde{\mathbf{v}}$, and $\tilde{e}$. The realizability conditions [4, 26] immediately follow from the Grammian features of $\mathbf{B}$ and so the necessary and sufficient conditions for $\mathbf{B} \in P\mathrm{sym}$ can be compactly expressed as $\frac{1}{2}\mathrm{tr}\mathbf{B} \geq 0$, $\frac{1}{2}[\bar{\rho}k^2 - \|\mathbf{B}\|^2] \geq 0$, and $\det\mathbf{B} \geq 0$.

Since the SGS eddies tend to be more homogeneous and isotropic than the large ones, eddy-viscosity models are often employed for their parameterization [1, 28]. In these, $\mathbf{B} = \frac{2}{3}\bar{\rho}k\mathbf{I} - 2\mu_k\tilde{\mathbf{D}}_D$ and $\mathbf{b} = -2\kappa_k\nabla\tilde{e}$, where k is the SGS kinetic energy, μ_k the SGS eddy viscosity, and κ_k the SGS eddy diffusivity. Among the eddy-viscosity models we find the Smagorinsky model (SMG) [29], with $k = c_{|}\Delta^2\|\tilde{\mathbf{D}}\|$, $\mu_k = c_D\bar{\rho}\,\Delta^2\|\tilde{\mathbf{D}}\|$, and $\kappa_k = \mu_k/Pr_T$, where $c_{|}$, c_D, and Pr_T are model coefficients left to be determined either from the assumption of isotropy and a $|\mathbf{k}|^{-5/3}$ inertial subrange behavior, or by the dynamic approach

(DSMG) [30], in which these are estimated locally using a "test" filter with a width of 2Δ. Alternatively, one-equation eddy-viscosity models (OEEVM) [31, 32] may be used in which k is obtained from $\partial_t(\bar{\rho}k) + \nabla\cdot(\bar{\rho}k\tilde{\mathbf{v}}) = -\mathbf{B}\cdot\tilde{\mathbf{D}} + \nabla\cdot(\mu\nabla k) + \bar{\rho}\varepsilon$, with $\varepsilon = c_\varepsilon k^{3/2}/\Delta$ and $\mu_k = c_k\bar{\rho}\,\Delta\sqrt{k}$. Values of the model coefficients c_k and c_ε can be obtained from either a $|\mathbf{k}|^{-5/3}$ inertial subrange behavior [31] or a dynamic approach [32]. For wall-bounded flows, damping functions are required when using the static method of calculating c_1, c_D, and Pr_T. Typically, these methods reduce the value of c_D when approaching the wall using a van Driest-type function, i.e., $c_D = c_D^0(1 - \exp(-y^+/A^+))$. A better alternative is, however, to calculate the coefficients from a Pao spectrum, $E(|\mathbf{k}|) = c_K\varepsilon^{2/3}|\mathbf{k}|^{-5/3}\exp(-\frac{3}{2}c_K|\mathbf{k}|^{-4/3})$, that includes the viscous subrange, resulting in $c_D \approx 0.027\times 10^{-3.23\cdot \mathrm{Re}_\Delta^{-0.92}}$, where $\mathrm{Re}_\Delta = \Delta^2\|\tilde{\mathbf{D}}\|/\nu$ is the grid Re number. The principal drawback in the dynamic method for evaluating the model coefficients is the use of ad hoc averaging in space or over time and additional clipping to limit the fluctuations in c_D and c_1. Physical-space stretched–vortex subgrid-stress models have been also proposed, capable of providing explicit estimates of the subgrid kinetic energy without a priori adjustable parameters, based on certain assumptions about the SGS vorticity structure [33].

Alternatives to the eddy-viscosity approach include scale-similarity models (SSM) [34, 35] and differential stress models (DSM) [36]. The probably most renowned SSM is that of Bardina *et al.* [34], in which the SGS stress tensor and flux vector are modeled as a linear combination of a SSM and a SMG model, i.e., $\mathbf{B} = \bar{\rho}(\widetilde{\tilde{\mathbf{v}}\otimes\tilde{\mathbf{v}}} - \tilde{\tilde{\mathbf{v}}}\otimes\tilde{\tilde{\mathbf{v}}}) + \frac{2}{3}\bar{\rho}k\mathbf{I} - 2\mu_k\tilde{\mathbf{D}}_D$ and $\mathbf{b} = \bar{\rho}(\widetilde{\tilde{\mathbf{v}}\tilde{e}} - \tilde{\tilde{\mathbf{v}}}\tilde{\tilde{e}}) - 2\kappa_k\nabla\tilde{e}$, typically improving considerably the correlations between exact and modeled SGS stresses in an a priori analysis [37]. For a posteriori analysis, however, neither the SSM nor the mixed model have improved predictions as much as hoped for. The earliest DSM was proposed by Deardorff [36], and examined by Fureby *et al.* [38]; it uses a modeled version of the balance equation for $\mathbf{B}$, i.e.,

$$\begin{aligned}\partial_t(\mathbf{B}) + \nabla\cdot(\mathbf{B}\otimes\tilde{\mathbf{v}}) \;=\; & -(\tilde{\mathbf{L}}\mathbf{B}^T + \mathbf{B}\tilde{\mathbf{L}}^T) + \nabla\cdot(\nu_k\nabla\mathbf{B}) \\ & - (c_M/\Delta)k^{1/2}\mathbf{B}_D + \frac{2}{5}\bar{\rho}k\tilde{\mathbf{D}}_D + \frac{2}{3}\bar{\rho}\varepsilon\mathbf{I},\end{aligned} \tag{2}$$

where $\mu_k = c_k\bar{\rho}\,\Delta\sqrt{k}$ and $\varepsilon = c_\varepsilon k^{3/2}/\Delta$. The principal advantage of the DSM over SMG and OEEVM is a built-in capacity for handling simultaneous grid and flow anisotropies, which is particularly important in complex wall-bounded flows. A similar model can be developed for $\mathbf{b}$. Assuming the SGS flow to be homogeneous and in equilibrium implies that the anisotropy of $\mathbf{B}$ ($\mathbf{A} = (\mathbf{B} - \frac{2}{3}\bar{\rho}k\mathbf{I})/2k$) achieves equilibrium values that are independent of the initial conditions, i.e., $\dot{\mathbf{A}} = 0$ (where the dot denotes the material time derivative), so that the DSM model (2) has the equilibrium form

$$\mathbf{B} = \frac{2}{3}\bar{\rho}k\mathbf{I} - \frac{2}{5}\mu_k\tilde{\mathbf{D}}_D - \beta\tau(\tilde{\mathbf{L}}\mathbf{B}^T + \mathbf{B}\tilde{\mathbf{L}}^T), \tag{3}$$

where $\tau = c_1/\|\tilde{\mathbf{D}}\|$ and $\beta = 1/(-\Delta(\mathbf{B}\cdot\tilde{\mathbf{D}}/k^{3/2}) - 1 + c_2)$ with $c_1 = O(1)$ and $c_2 = O(1)$ being model coefficients related to c_k, c_M, and c_ε. This algebraic stress model (ASM) consists of two parts: an eddy-viscosity part and a nonlinear implicit part related to the production of $\mathbf{B}$. The ASM is particularly interesting in light of the recent studies of Shao *et al.* [19] demonstrating the partition of $\mathbf{B}$ into a rapid part (dependent on $\tilde{\mathbf{L}}$) and a slow part (independent of $\tilde{\mathbf{L}}$). Here, the rapid part, which cannot be captured by isotropic models,

corresponds to $\mathbf{B}^{(2)} = \beta\tau(\tilde{\mathbf{L}}\mathbf{B}^T + \mathbf{B}\tilde{\mathbf{L}}^T)$, which is essentially the production of $\mathbf{B}$, and the slow part corresponds to the term $\mathbf{B}^{(1)} = \frac{2}{3}\bar{\rho}k\mathbf{I} - \frac{2}{5}\mu_k\tilde{\mathbf{D}}_D$.

3. NUMERICAL METHODS FOR CONVENTIONAL LES

LES requires high-order schemes to avoid masking the SGS terms (div$\mathbf{B}$ and div$\mathbf{b}$) by the leading-order truncation error. In general, $\mathbf{B}$ and $\mathbf{b}$ are proportional to Δ^p, where $4/3 < p < 2$ (e.g. [5]). The filter width Δ is usually related to the grid, so that $\Delta \propto |\mathbf{d}|$, where $|\mathbf{d}|$ is the grid size, which formally makes the modeled SGS stresses and fluxes $O(|\mathbf{d}|^p)$ terms. In LES, spectral, pseudospectral, and high-order finite volume or difference methods are used for spatial discretization, and explicit semi-implicit or predictor–corrector methods of at least second-order accuracy are used for time integration. In addition, LES is formally not filtered in time and should therefore be fully resolved with $\Delta t < \tau_K$, where Δt is the time step and τ_K the Kolmogorov time. However, since only the large scales are retained, requiring the Courant number to satisfy $\mathrm{Co} < 0.2$ is sufficient.

To illustrate the discretization of the LES equations we use the finite volume (FV) method in which the domain D is partitioned into cells Ω_P so that $\cup_P(\Omega_P) = D \cup \partial D$ and $\cap_P(\Omega_P) = \varnothing$. By defining the approximation to the cell average of f over the Pth cell by $f_P = \frac{1}{\delta V_P}\int_{\Omega_P} f\,dV$, Gauss theorem may be used to derive the semidiscretized LES equations. By integrating these over time using a conventional multistep method, [39], the discretized LES equations become

$$\begin{cases} \sum_{i=0}^{m}\left(\alpha_i \bar{\rho}_P^{n+i} + \frac{\beta_i \Delta t}{\delta V_P}\sum_f \left[F_f^{C,\rho}\right]^{n+i}\right) = 0, \\ \sum_{i=0}^{m}\left(\alpha_i(\bar{\rho}\tilde{\mathbf{v}})_P^{n+i} + \frac{\beta_i \Delta t}{\delta V_P}\sum_f \left[\mathbf{F}_f^{C,v} + \mathbf{F}_f^{D,v} + \mathbf{F}_f^{1,v} + \mathbf{F}_f^{2,v} + \mathbf{F}_f^{B,v}\right]^{n+i}\right) \\ \quad = -\beta_i(\nabla \bar{p})_P^{n+i}\Delta t + \beta_i(\bar{\rho}\tilde{\mathbf{f}})_P^{n+i}\Delta t, \\ \sum_{i=0}^{m}\left(\alpha_i(\bar{\rho}\tilde{e})_P^{n+i} + \frac{\beta_i \Delta t}{\delta V_P}\sum_f \left[F_f^{C,e} + F_f^{D,e} + F_f^{b,e}\right]^{n+i}\right) \\ \quad = \beta_i(\bar{\mathbf{S}}\cdot\tilde{\mathbf{D}} + \bar{\rho}\varepsilon + \bar{\rho}\tilde{\sigma})_P^{n+i}\Delta t, \end{cases} \tag{4}$$

where m, α_i, and β_i are parameters of the time-integration scheme, and where

$$\begin{cases} F_f^{C,\rho} = (\bar{\rho}\tilde{\mathbf{v}}\cdot d\mathbf{A})_f, \quad \mathbf{F}_f^{C,v} = (\bar{\rho}\tilde{\mathbf{v}}\cdot d\mathbf{A})_f\tilde{\mathbf{v}}_f, \quad F_f^{C,e} = (\bar{\rho}\tilde{\mathbf{v}}\cdot d\mathbf{A})_f\tilde{e}_f, \\ \mathbf{F}_f^{D,v} = (\mu\nabla\tilde{\mathbf{v}})_f d\mathbf{A}, \quad \mathbf{F}_f^{1,v} = (\lambda\nabla\cdot\tilde{\mathbf{v}})_f d\mathbf{A}, \quad \mathbf{F}_f^{2,v} = (\mu\nabla\tilde{\mathbf{v}}^T)_f d\mathbf{A}, \quad \mathbf{F}_f^{B,v} = \mathbf{B}_f d\mathbf{A}, \\ F_f^{D,e} = \left(\frac{\kappa}{C_v}\nabla\tilde{e}\right)_f \cdot d\mathbf{A}, \quad F_f^{b,e} = \mathbf{b}_f \cdot d\mathbf{A} \end{cases} \tag{5}$$

are the convective, viscous and diffusive, and auxiliary fluxes from the continuity, momentum, and energy equations. To complete the FV discretization, all fluxes, defined at cell faces f, need to be reconstructed from the dependent variables at adjacent cells. This requires flux interpolation for the convective fluxes and difference approximations for the inner derivatives in the other fluxes. The discretization of the inner derivatives typically involves central differencing of second- or fourth-order accuracy, while the functional reconstruction of the convective terms accordingly involves linear or cubic interpolations, resulting in second- or fourth-order-accurate central schemes, respectively. For example,

for second-order accuracy, $O(\mathbf{d}^2)$, we typically use

$$\begin{cases} \mathbf{F}_f^{C,v} = \mathbf{F}_f^{C,\rho}\tilde{\mathbf{v}}_f = \mathbf{F}_f^{C,\rho}\left(\ell\tilde{\mathbf{v}}_P + (1-\ell)\tilde{\mathbf{v}}_N - \frac{1}{8}(\mathbf{d}\otimes\mathbf{d})\nabla^2\tilde{\mathbf{v}} + \cdots\right), & \text{(6a)} \\ \mathbf{F}_f^{D,v} = \mu|d\mathbf{A}|(\tilde{\mathbf{v}}_N - \tilde{\mathbf{v}}_P)/|\mathbf{d}| + \frac{1}{6}\mu(\mathbf{d}\otimes\mathbf{d})\nabla^3\tilde{\mathbf{v}} + \cdots, & \text{(6b)} \end{cases}$$

where $\frac{1}{6}\mu(\mathbf{d}\otimes\mathbf{d})\nabla^3\tilde{\mathbf{v}}$ and $-\frac{1}{8}(\mathbf{d}\otimes\mathbf{d})\nabla^2\tilde{\mathbf{v}}$ represent the leading-order truncation errors. In order to examine the effects of the discretization we study the equivalent or modified equations, i.e., the partial differential equations satisfied by the numerical solution. These equations may be obtained as the discretized equations are assembled, simply by recognizing the discretized forms of the involved operators and by including the leading-order truncation errors, viz.,

$$\begin{cases} \partial_t(\bar{\rho}) + \nabla\cdot(\bar{\rho}\tilde{\mathbf{v}}) = 0, \\ \partial_t(\bar{\rho}\tilde{\mathbf{v}}) + \nabla\cdot(\bar{\rho}\tilde{\mathbf{v}}\otimes\tilde{\mathbf{v}}) = -\nabla\bar{p} + \nabla\cdot(\bar{\mathbf{S}} - \mathbf{B}) + \bar{\rho}\tilde{\mathbf{f}} + \nabla\cdot\left\{(\mathbf{d}\otimes\mathbf{d})\right. \\ \qquad\qquad \left.\times\left[-\frac{1}{8}\nabla^2\tilde{\mathbf{v}} + \frac{1}{6}\mu\nabla^3\tilde{\mathbf{v}}\right] + \cdots\right\}, \\ \partial_t(\bar{\rho}\tilde{e}) + \nabla\cdot(\bar{\rho}\tilde{e}\tilde{\mathbf{v}}) = \nabla\cdot(\bar{\mathbf{h}} - \mathbf{b}) + \bar{\mathbf{S}}\cdot\tilde{\mathbf{D}} + \bar{\rho}\varepsilon + \bar{\rho}\tilde{\sigma} + \nabla\cdot\left\{(\mathbf{d}\otimes\mathbf{d})\right. \\ \qquad\qquad \left.\times\left[-\frac{1}{8}\nabla^2\tilde{e} + \frac{1}{6}\kappa\nabla^3\tilde{e}\right] + \cdots\right\}, \end{cases} \tag{7}$$

where the last terms on the right hand side represent the truncation error. Note that if the spatial discretization is pth-order accurate, then the leading-order truncation error is proportional to $\mathbf{d}^p$. When this term is dominated by odd-order spatial derivatives, numerical dispersion occurs, causing unphysical oscillations in the solution—which will need to be damped out. Often, artificial viscosity is introduced for this purpose but for LES the explicit SGS model is preferable and should be sufficient to damp these oscillations. On the other hand, if even-order derivatives dominate, numerical diffusion is added to the solution. In (7), odd- and even-order derivatives coexist, with dispersion dominating over the hyperviscosity terms [40]. Equations (7) reveal the competition between leading-order truncation errors and the specific SGS model and may be used to investigate the properties to be anticipated from the overall LES model. In the absence of an explicit SGS model, (7) can be likewise used to address the extent to which leading-order truncation errors may provide an implicit SGS model if suitable algorithms are used.

4. MONOTONICALLY INTEGRATED LES (MILES)

Formal drawbacks of conventional LES models include the assumption that the commutation error is negligible or can be modeled, the possible masking of the SGS flux terms by leading-order truncation errors, and difficulties associated with formulating (explicit) SGS models. The task of formulating computational fluid dynamics models involves both numerical and physical trade-offs, and the accuracy of the model is not better than its weakest part. With this regard it is important to consider not only physical and numerical aspects but also their combined effects. Sophisticated SGS models and advanced numerical methods have been developed for LES and successfully applied to different flow problems, but not very often has the overall computational model, i.e., the modified equations, been used as basis for improved LES. Although the history of MILES draws on the development of shock-capture schemes [20], the concept of MILES, as developed in [22, 23], attempts to

embody a computational procedure for solving the NSE as accurately as possible using built-in, or implicit, SGS models. Because of the anisotropic features of the SGS modeling in MILES [23], with possibilities of simultaneously handling flow and grid anisotropies, this may simply provide a better approach for inhomogeneous turbulent flows.

Compared to conventional LES, where the SGS effects are represented by explicit SGS models, MILES uses the features of particular numerical methods to construct implicit SGS models by means of the leading-order truncation error [41]. By incorporating a sharp velocity-gradient-capture capability operating at the smallest resolved scales, with MILES we seek to emulate (near the cutoff) the high-wavenumber end of the inertial subrange region—characterized by thin filaments of intense vorticity embedded in a background of weak vorticity [6–11]. MILES draws on the fact that finite difference, volume, and element methods filter the NSE over cells Ω_P, with characteristic dimension $|\mathbf{d}|$—using a top-hat-shaped kernel $f_P = \frac{1}{\delta V_P}\int_{\Omega_P} f\,dV$. In the FV context the semidiscretized MILES equations can be obtained from the NSE using Gauss' theorem, viz.,

$$\begin{cases} \sum_{i=0}^{m}\left(\alpha_i \rho_P^{n+i} + \frac{\beta_i \Delta t}{\delta V_P}\sum_f \left[F_f^{C,\rho}\right]^{n+i}\right) = 0, \\ \sum_{i=0}^{m}\left(\alpha_i (\rho \mathbf{v})_P^{n+i} + \frac{\beta_i \Delta t}{\delta V_P}\sum_f \left[\mathbf{F}_f^{C,v} + \mathbf{F}_f^{D,v} + \mathbf{F}_f^{1,v} + \mathbf{F}_f^{2,v}\right]^{n+i}\right) \\ \quad = -\beta_i (\nabla p)_P^{n+i}\Delta t + \beta_i (\rho \mathbf{f})_P^{n+i}\Delta t, \\ \sum_{i=0}^{m}\left(\alpha_i (\rho e)_P^{n+i} + \frac{\beta_i \Delta t}{\delta V_P}\sum_f \left[F_f^{C,e} + F_f^{D,e}\right]^{n+i}\right) = \beta_i (\mathbf{S}\cdot\mathbf{D} + \rho\sigma)_P^{n+i}\Delta t, \end{cases} \tag{8}$$

where the convective, viscous, diffusive, and auxiliary fluxes are defined by

$$\begin{cases} F_f^{C,\rho} = (\rho \mathbf{v}\cdot d\mathbf{A})_f, \quad \mathbf{F}_f^{C,v} = (\rho \mathbf{v}\cdot d\mathbf{A})_f \mathbf{v}_f, \quad F_f^{C,e} = (\rho \mathbf{v}\cdot d\mathbf{A})_f e_f, \\ \mathbf{F}_f^{D,v} = (\mu \nabla \mathbf{v})_f d\mathbf{A}, \quad \mathbf{F}_f^{1,v} = (\lambda \nabla\cdot \mathbf{v})_f d\mathbf{A}, \quad \mathbf{F}_f^{2,v} = (\mu(\nabla \mathbf{v})^T)_f d\mathbf{A}, \\ F_f^{D,e} = \left(\frac{\kappa}{C_V}\nabla e\right)_f \cdot d\mathbf{A}. \end{cases} \tag{9}$$

To complete the discretization, all fluxes at face f need to be reconstructed from the dependent variables at adjacent cells. This requires flux interpolation for the convective fluxes and difference approximations for the inner derivatives in the other fluxes. Given (8) and (9) the methods available for constructing implicit SGS models by means of the leading-order truncation errors are generally restricted to nonlinear "high-resolution" methods for the convective fluxes $\mathbf{F}_f^{C,v}$ and $\mathbf{F}_f^{C,e}$, in order to maintain at least second-order accuracy in smooth regions of the flow [42]. The term high-resolution applies to methods that are at least second-order accurate on smooth solutions and yet give well-resolved, nonoscillatory discontinuities. In addition, these schemes are required to provide a leading-order truncation error that vanishes as $\mathbf{d} \to \mathbf{0}$, so that it remains consistent with the NSE and the conventional LES model (1). There are a wide variety of approaches that can be taken (e.g. [39–41]), but here we will focus on flux-limiting/correcting methods.

In this approach, we introduce a flux limiter $\Gamma = \Gamma(\mathbf{v}(\mathbf{x}, t))$ to combine a high-order convective flux function $\mathbf{v}_f^H$, which is well-behaved in smooth flow regions, with a low-order dispersion-free convective flux-function $\mathbf{v}_f^L$, being well behaved near sharp gradients, so that the total convective flux function becomes $\mathbf{v}_f = \mathbf{v}_f^H - (1-\Gamma)[\mathbf{v}_f^H - \mathbf{v}_f^L]$. Typically, $\mathbf{v}_f^H$ is obtained from linear or cubic interpolations, resulting in second- or fourth-order-accurate central schemes, respectively, while $\mathbf{v}_f^L$ is obtained from an upwind-biased piecewise constant

approximation, i.e.,

$$\begin{cases} \mathbf{F}_f^{C,v,H} = F_f^{C,\rho}\left[\ell\mathbf{v}_P + (1-\ell)\mathbf{v}_N - \frac{1}{8}(\mathbf{d}\otimes\mathbf{d})\nabla^2\mathbf{v} + \cdots\right], \\ \mathbf{F}_f^{C,v,L} = F_f^{C,\rho}[\beta^+\mathbf{v}_P + \beta^-\mathbf{v}_N + (\beta^+ - \beta^-)(\nabla\mathbf{v})\mathbf{d} + \cdots], \\ \beta^\pm = \frac{1}{2}(\mathbf{v}_f\cdot d\mathbf{A} \pm |\mathbf{v}_f\cdot d\mathbf{A}|)/|\mathbf{v}_f\cdot d\mathbf{A}|, \end{cases} \tag{10}$$

where λ is the distance function, and $-\frac{1}{8}(\mathbf{d}\otimes\mathbf{d})\nabla^2\mathbf{v}$ and $(\beta^+ - \beta^-)(\nabla\mathbf{v})\mathbf{d}$ are the leading-order truncation errors. The flux limiter $\mathbf{\Gamma}$ is thus to be formulated to allow as much as possible of the correction or antidiffusion term $[\mathbf{v}_f^H - \mathbf{v}_f^L]$ to be included without increasing the variation of the solution—e.g., to comply with the physical principles of causality, monotonicity, and positivity (when applicable) (cf. [20, 22]), and thus to preserve the properties of the NSE. Flux-limiting schemes are more accurate than comparable conventional schemes; for example, the FCT schemes used in this paper are second-order accurate in amplitude and fourth-order phase accurate [20], based on their formal properties in smooth regions (where the higher order scheme is active), while the concept of accuracy based on Taylor series is actually meaningless near discontinuities (where the lower order scheme is active).

To see the effects of this convection discretization we consider the modified equations corresponding to the semidiscretized equations (8) and (9), using the flux functions (6b) and (10) for the viscous, diffusive, auxiliary, and convective fluxes, respectively,

$$\begin{cases} \partial_t(\rho) + \nabla\cdot(\rho\mathbf{v}) = 0, \\ \partial_t(\rho\mathbf{v}) + \nabla\cdot(\rho\mathbf{v}\otimes\mathbf{v}) = -\nabla p + \nabla\cdot\mathbf{S} + \rho\mathbf{f} + \nabla\cdot\left\{\rho(\mathbf{C}\mathbf{L}^T + \mathbf{L}\mathbf{C}^T + \chi^2\mathbf{L}\mathbf{d}\otimes\mathbf{L}\mathbf{d})\right. \\ \qquad\qquad \left. + \frac{1}{6}\mu(\mathbf{d}\otimes\mathbf{d})\nabla^3\mathbf{v} + \cdots\right\}, \\ \partial_t(\rho e) + \nabla\cdot(\rho\mathbf{v}e) = \nabla\cdot\mathbf{h} + \mathbf{S}\cdot\mathbf{D} + \rho\sigma + \nabla\cdot\left\{\rho(\mathbf{C}\nabla e + \chi^2(\nabla e\cdot\mathbf{d})\mathbf{L}\mathbf{d})\right. \\ \qquad\qquad \left. + \frac{1}{6}\kappa(\mathbf{d}\otimes\mathbf{d})\nabla^3 e + \cdots\right\}, \end{cases} \tag{11}$$

where $\mathbf{C} = \chi(\mathbf{v}\otimes\mathbf{d})$ and $\chi = \frac{1}{2}(1-\Gamma)(\beta^- - \beta^+)$. Compared to the NSE (1), the discretization has introduced additional dissipative and dispersive terms, from which we can identify the implicit (or built-in) SGS terms as $\mathbf{B} = \rho(\mathbf{C}\mathbf{L}^T + \mathbf{L}\mathbf{C}^T + \chi^2\mathbf{L}\mathbf{d}\otimes\mathbf{L}\mathbf{d})$ and $\mathbf{b} = \rho(\mathbf{C}\nabla e + \chi^2(\nabla e\cdot\mathbf{d})\mathbf{L}\mathbf{d})$. The implicit SGS stress tensor can be split into $\mathbf{B}^{(1)} = \rho(\mathbf{C}\mathbf{L}^T + \mathbf{L}\mathbf{C}^T)$ and $\mathbf{B}^{(2)} = \rho\chi^2(\mathbf{L}\mathbf{d}\otimes\mathbf{L}\mathbf{d})$, of which the former is a generalized eddy-viscosity model with $\mathbf{C}$ being a tensor-valued eddy viscosity, while the latter is of a form similar to the SSM part in the mixed model of Bardina *et al.* [34]. This decomposition is also attractive considering the decomposition into rapid and slow parts suggested by Shao *et al.* [19]. In MILES, the rapid part that cannot be captured by isotropic models relates to $\mathbf{B}^{(2)}$ and $\mathbf{b}^{(2)} = \rho\chi^2(\nabla e\cdot\mathbf{d})\mathbf{L}\mathbf{d}$, while the slow part relates to $\mathbf{B}^{(1)}$ and $\mathbf{b}^{(1)} = \rho\mathbf{C}\nabla e$. Borue and Orszag [43] have shown that a $\mathbf{B}^{(2)}$-type term improves the correlations between the exact and the modeled SGS stress tensor.

The detailed properties of the implicit SGS model are thus closely related to the formulation of the flux limiter Γ, and the resulting properties of the scheme. To examine these properties, we consider the one-dimensional continuity equation $\partial_t(\rho) + \partial_x(\rho v) = 0$, $v > 0$. Discretization using the FV method in conjunction with the flux-limiter formulation $\rho_f = \rho_f^H - (1-\Gamma)[\rho_f^H - \rho_f^L]$ and the flux functions (6b) and (10) yields $\rho_P^{n+1} = \rho_P^n - \upsilon[(1 - \frac{1}{2}\Gamma_{P-1/2})\delta\rho_{P-1/2}^n - \frac{1}{2}\Gamma_{P+1/2}\delta\rho_{P+1/2}^n] = -C\delta\rho_{P-1/2}^n + D\delta\rho_{P+1/2}^n$, where $\upsilon = v\Delta t/\Delta x$, $\delta\rho_{P-1/2}^n = \rho_P^n - \rho_{P-1}^n$, and $\delta\rho_{P+1/2}^n = \rho_{P+1}^n - \rho_P^n$. After Harten [44], a method of this

form is total variation diminishing (TVD), i.e., $\mathrm{TV}(\rho^{n+1}) \le \mathrm{TV}(\rho^n)$, where the total variation is defined by $\mathrm{TV}(\rho^n) = \Sigma_P |\rho^n_{P+1} - \rho^n_P|$, if and only if $C \ge 0$, $D \ge 0$, and $C + D \le 1$. These inequalities are simultaneously satisfied if $0 \le |\Gamma(r), \Gamma(r)/r| \le 2$, where $r = \delta\rho^n_{P-1/2}/\delta\rho^n_{P+1/2} = (\rho^n_P - \rho^n_{P-1})/(\rho^n_{P+1} - \rho^n_P)$ is the ratio of consecutive gradients. To achieve second-order accuracy we must further require that $\Gamma(l) = 1$ and that Γ be Lipschitz continuous in r. Possible associated constraints on a scheme prescribed by $\rho^{n+1}_P = H(\rho^n_{P-k}, \rho^n_{P-k+1}, \ldots, \rho^n_{P+k})$ include the following:

(i) monotonicity, $\partial H/\partial\rho^n_j \ge 0$ for all $P - k \le j \le P + k$;

(ii) l_1-contraction, $\|\rho^{n+1}_P - \tilde{\rho}^{n+1}_P\|_1 \le \|\rho^n_P - \tilde{\rho}^n_P\|_1$, where ρ and $\tilde{\rho}$ are solutions to the same equation with different initial data, and where $\|\cdot\|_1$ denotes the l_1-norm;

(iii) (local) monotonicity preservation, i.e., if $\rho^0_P \ge \rho^0_{P+1}$ then $\rho^n_P \ge \rho^n_{P+1}$ for all P and n.

In particular, it is clear that a monotone method is also l_1-contracting, and hence also TVD, which further implies that the scheme is monotonicity preserving. The detailed implications of these constraints on MILES are not yet completely clear but are under investigation [45]. Based on our accumulated experience, monotone and l_1-contracting methods are generally too diffusive, whereas some TVD methods (e.g., using the SUPERBEE limiter [46]) and most monotonicity preserving methods (e.g., FCT and the Gamma limiter [47]) work very well for MILES.

Comparative studies using MILES and conventional LES applied to compressible free shear flows, i.e., forced homogeneous isotropic turbulence, have previously been undertaken [6, 23]. It was found that both MILES and conventional LES work well provided that (i) the cutoff wavenumber, $\mathbf{k}_C$, lies within the inertial subrange, and (ii) the combined model-algorithm-discretization can adequately channel kinetic energy out of wavenumbers close to $\mathbf{k}_C$ in order to prevent spurious energy buildup and aliasing. For high-Re-free shear flows, the comparisons indicate that the MILES approach is generally not worse than conventional LES and, in fact, they suggest that MILES tends to compare favorably for higher Re or improved resolution once $\mathbf{k}_C$ lies within the inertial subrange [6, 23]. These trends are confirmed in the applications discussed below.

5. CASE STUDIES

Formal properties of the effective SGS modeling using MILES are documented in what follows, using databases of simulated free and wall-bounded flows. The approach was tested in a broad range of representative applications, including homogeneous isotropic decaying turbulence, transitional jets, and channel flows. The numerical methods used in the simulations are based on Eqs. (4)–(6) or (8)–(10), depending on whether conventional LES or MILES is used.

5.1. *Decaying Isotropic Turbulence*

As a first test case we attempt to simulate the experiment on decaying turbulence behind a grid studied by Comte-Bellot and Corrsin [48]. In the experiments, turbulence is generated behind a periodic array of square rods, in a biplane arrangement, forming a grid with a solidity of 0.34. The grid is inserted in a rectangular ($1.37 \times 1.03\,\mathrm{m}^2$) wind tunnel section and the measurements are taken further downstream, after a contraction of 1.27 : 1 to improve the isotropy of the turbulence. According to the measurements, the turbulence was very

nearly isotropic, with the ratio of streamwise and transverse rms velocity fluctuations in the range of 0.97 to 0.98. In the simulations we consider the case with the grid Re number of $\mathrm{Re}_M = U_0 M/\nu = 34{,}000$, where U_0 is the freestream velocity and M the grid spacing, and we compare one-dimensional energy spectra from SMG, DSM, and MILES with measured spectra at times $tU_0/M = 42$, 98, and 171, corresponding to Taylor Reynolds numbers of $\mathrm{Re}_\lambda = 71.6$, 65.3, and 60.7, respectively. The simulations are carried out in a box with a size larger than the integral scale and much smaller than the wind tunnel cross section (advected with the average flow) with periodic boundary conditions. The initial velocity field is created by superimposing Fourier modes having a prescribed energy spectrum but random phases and projecting these onto the divergence free space (cf. [6]).

Simulations were performed at 32^3 and 64^3 resolutions with all SGS models. Figure 1 shows the evolution of the energy spectrum from SMG, DSM, and MILES at both resolutions compared to the experimental data of Comte-Bellot and Corrsin [48]. The decay rate of the energy spectra is predicted equally well by all models; improving resolution has the effect of extending the captured portion of the inertial subrange in similar ways for all models (i.e., the approximate LES cutoffs in Fig. 1 move similarly from $k \sim 1.4$ to ~ 3, respectively, for the 32^3 and 64^3 resolutions).

Two additional calculations (one on each grid) were performed, using the numerics described in (4)–(6) with the explicit (SMG or DSM) SGS models switched off. In both cases the simulation failed due to a rather rapid buildup of energy close to the cutoff wavenumber $\mathbf{k}_C$. The failure of these *particular* "no-model" simulation approaches thus tested, based on (4)–(6), was previously noted, e.g., in simulations of forced homogeneous isotropic turbulence [6, 23], and also in simulations of more complex flows such as the channel flow simulations reported below. From the point of view of the modified LES equation (7), this failure indicates the inadequacy of the implicit SGS model associated with (4)–(6). In MILES, physical energy drainage close to $\mathbf{k}_C$ can be effectively enforced (Fig. 1) because of the special nature of the implicit SGS model involved—discussed above in connection with (11).

5.2. *Transitional Free Jets*

Here we focus on modeling the transition to turbulence in free rectangular jets evolving from laminar initial conditions. As in [49], the simulated low aspect ratio (AR = 1–3) jets are initialized with a thin vortex sheet having slightly rounded-off corner regions and uniform initial momentum thickness θ. The simulations focus on the transitional vortex dynamics downstream of the jet exit, when low initial turbulence intensities are involved, and when azimuthal nonuniformities in θ and the streamwise vorticity at the jet exit can be regarded as negligible. Inflow and outflow conditions are imposed at the open boundaries in the streamwise direction and stagnant flow conditions are imposed at the cross-stream boundaries. Axial forcing is implemented to facilitate the analysis of the results by superimposing on the free jet velocity U_j an axial, time-dependent sinusoidal perturbation of 2.5% rms of U_j. This forcing involves a nondimensional Strouhal frequency, $f D_e/U_j = 0.5$ (consistent with observed jet preferred frequencies in laboratory experiments), where D_e is the jet equivalent diameter, defined as the diameter of a circular jet with the same cross-sectional area.

The Cartesian computational grids used in the computational studies consisted of evenly spaced cells in the shear flow region and geometrical stretching in the cross-stream direction outside the core flow, used to implement the open boundary conditions (Fig. 2a). The grids

were held fixed in time with Co = 0.5, and typically employed between 120×87^2 (cell size 2Δ) and 240×174^2 (cell size Δ) computational cells with $\Delta = D/42$, where D is the length of the minor side of the jet cross section. The simulations reported here were performed on an intermediate-resolution grid with cell size 1.5Δ using between 150×110^2 and 200×190^2 cells. The full computational domain had a streamwise extent of approximately $7D_e$ and extended up to $\pm 5D_e$ away from the jet axis in both transverse directions. A one-dimensional FCT scheme is used in the streamwise direction [51], two-dimensional FCT is used in the cross-stream planes [52], and three-dimensional central differences are used for the other local processes. Second-order-accurate FCT methods are used, while the time integration is a second-order-accurate predictor–corrector scheme.

The gas jets investigated emerge into a quiescent background with Ma number Ma = 0.6. The jet and background are composed of air at the same uniform initial temperature and pressure, and thermal effects are neglected. The jet simulations are based on either the unfiltered Euler equations (MILES-EU), or the NSE with or without SMG, which we denote MILES-SMG or MILES, respectively. In the case of MILES-EU the simulation is based on convection only; i.e., we assume that the flow can be regarded as virtually inviscid and isothermal, so the only viscosity involved is the residual viscosity of the FCT scheme [23]. In MILES we include the molecular viscosity but disregard the thermal effects—taking advantage of the virtually isothermal nature of the flow. In the MILES-SMG case we also superimpose the SMG viscosity—which is evaluated using the unfiltered flow velocities. Table I lists the jet simulations discussed in this section, where Re is based on D_e, U_j, and estimated upper bounds of the effective numerical viscosity of the FCT algorithm [53] (MILES-EU), or the molecular viscosity μ, otherwise.

Figure 2b is used to highlight the relevant differences between square and rectangular jets based on representative instantaneous volume visualizations, using ray tracing, of λ_2 and the streamwise vorticity $\omega_1 = (\nabla \times \mathbf{v})_1$ for jets with AR = 1 and 3. After Jeong and Hussain [54], the identification of vortex cores is based on λ_2, the second largest eigenvalue of the tensor $\mathbf{D}^2 + \mathbf{W}^2$, where $\mathbf{D}$ and $\mathbf{W}$ are the symmetric and skew-symmetric components of the velocity gradient $\mathbf{L} = \nabla \mathbf{v}$, since the tensor $\mathbf{D}^2 + \mathbf{W}^2$ determines the existence of a local pressure minimum due to vortical motion. The λ_2-visualization approach has been shown to be ideally suited for the investigation of complex vortex topologies [54–57]. The rectangular vortex ring dynamics for AR ≥ 2 [56] is essentially the same as that of pseudoelliptic [58] and elliptic [59] rings with the same AR, after the corner

TABLE I
Nominal Characteristic Parameters for the Free Jet Simulations

	Grid, cell-size	AR	Re	D_e/θ	St	Numerics
MILES-EU[a]	225×174^2, Δ	1	>220,000	75	0.55	$O(\Delta t^2, \mathbf{d}^2) + \text{FCT}$
MILES-EU[a]	112×87^2, 2Δ	1	>78,000	75	0.55	$O(\Delta t^2, \mathbf{d}^2) + \text{FCT}$
MILES	150×110^2, 1.5Δ	1	3,200	50	0.48	$O(\Delta t^2, \mathbf{d}^2) + \text{FCT}$
MILES-SMG	150×110^2, 1.5Δ	1	3,200	50	0.48	$O(\Delta t^2, \mathbf{d}^2) + \text{FCT}$
MILES-EU	150×110^2, 1.5Δ	1	>85,000	50	0.48	$O(\Delta t^2, \mathbf{d}^2) + \text{FCT}$
MILES-EU	200×190^2, 1.5Δ	1	>85,000	50	0.48	$O(\Delta t^2, \mathbf{d}^2) + \text{FCT}$
MILES-EU	200×190, 1.5Δ	2	>85,000	50	0.48	$O(\Delta t^2, \mathbf{d}^2) + \text{FCT}$
MILES-EU	200×190^2, 1.5Δ	3	>85,000	50	0.48	$O(\Delta t^2, \mathbf{d}^2) + \text{FCT}$

[a] Used in [23] to address grid resolution and convergence issues.

regions of the rings are effectively rounded in an early vortex-ring deformation phase. Two qualitatively different ring–rib coupling geometries are shown in Fig. 2b: jets with AR ≥ 2 are characterized by single ribs aligned with corner regions—in contrast to pairs of counterrotating ribs aligned with the corners for square jets. Other distinct topological features are associated with the occurrence of vortex ring splittings due to reconnection [50, 56, 58, 59]. In terms of characteristic ring–rib coupling geometry, significantly larger jet spreading and ω_1 vorticity production in the jet for AR $= 1$ are shown in Fig. 2b, reflecting the appearance of rib pairs aligned with corner regions—rather than single ribs for AR $= 3$. On the other hand, also associated with the larger near-jet ω_1 production for AR $= 1$, the vortex rings tend to be more unstable azimuthally and break down closer to the jet exit. As a consequence, Fig. 2b presents larger jet spreading for AR $= 3$ further downstream (say for $x > 6D_e$), where better entrainment properties are suggested by the more intense distributions of streamwise vorticity (much more intense for AR $= 3$ than for AR $= 2$). Furthermore, vortex self-deformation and axis switching

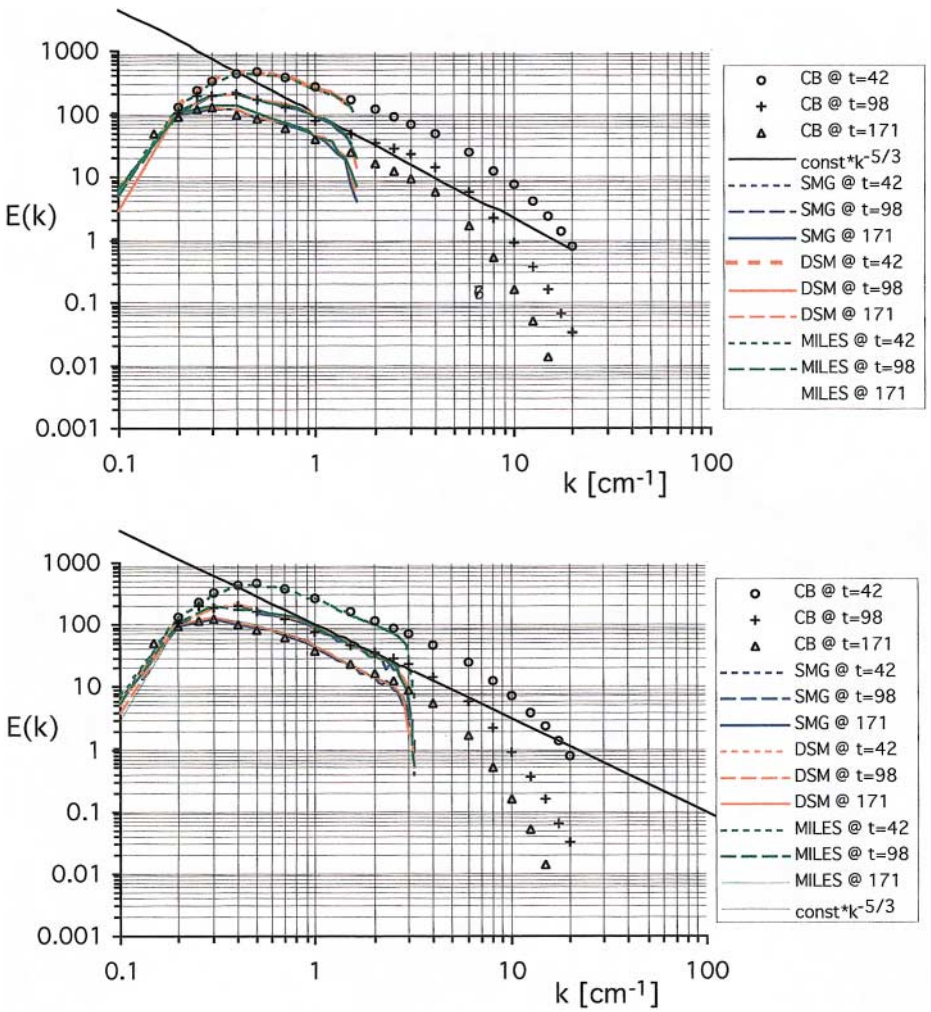

FIG. 1. Temporal evolution of the one-dimensional energy spectrum in 32^3 (top) and 64^3 (bottom) simulations of decaying isotropic turbulence, compared with measurements by Comte-Bellot [48].

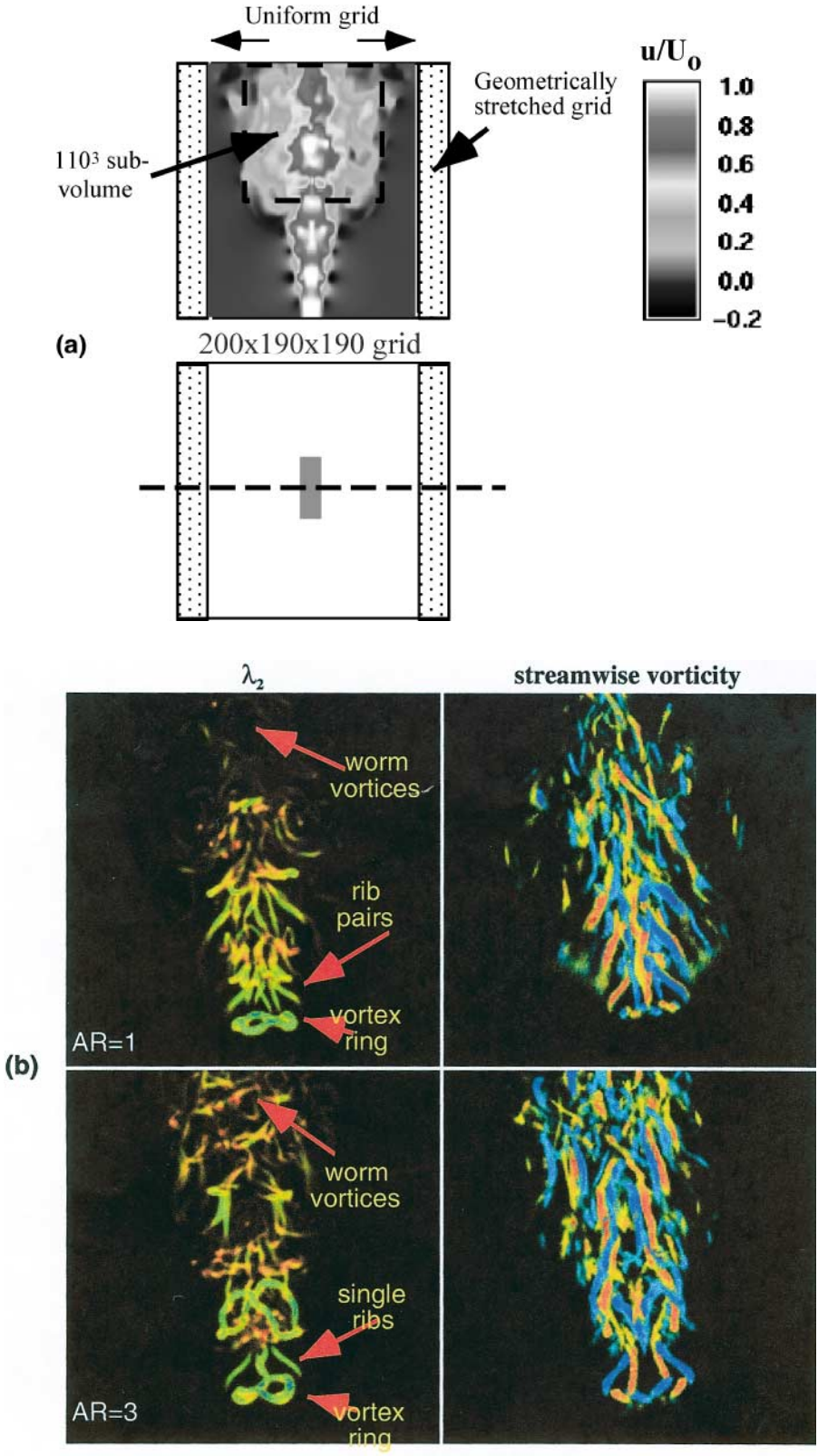

FIG. 2. (a) Example of computational domain used in the jet simulations. (b) Comparative instantaneous flow visualizations of simulated square and rectangular jets (same times and color mappings chosen).

can occur (and promote mixing better) closer to the jet exit for the AR = 1 case due to significantly smaller characteristic vortex-ring axis-switching times—i.e., typically half as large and less than one-third as large, respectively, compared with those for AR = 2 and 3 (e.g., [50]).

Next we make quantitative statements on the trends of the population of the small-scale vortices in the downstream portion of the jets, where the flow is characterized by thinner filament vortices similar to those observed in fully developed turbulent flows (e.g., [9–11]). Issues of grid resolution on MILES of free jets have previously been addressed [23] using data from the coarsest and the finest grids cited above. The analysis that follows concentrates on the transitional downstream portion of the jets and is used to compare the small-scale jet behavior captured by the simulations. To minimize the effects of transients, we focus on flow data for times $t > 3t_0$, where t_0 is the transit time for streamwise convection with velocity U_j across the computational domain.

In order to improve the basis for comparing current jet data with available DNS data of incompressible homogeneous isotropic turbulence, it is helpful to also base the analysis on the solenoidal component of the jet velocity data. The instantaneous velocity fluctuation can be decomposed into its solenoidal and compressible components according to $\mathbf{v} = \mathbf{v}^s + \mathbf{v}^c$, with the condition $\nabla \cdot (\mathbf{v}^s) = 0$ in physical space translating into the condition $\mathbf{k} \cdot \mathbf{v}^s = 0$ in Fourier space. This condition is explicitly used to obtain the solenoidal component of the Fourier velocity transform in the form $\mathbf{v}^s = \mathbf{v} - (\mathbf{v} \cdot \mathbf{k})\mathbf{k}/|\mathbf{k}|^2$, where by $\mathbf{v}^s$ is evaluated by means of an inverse Fourier transform. The solenoidal part of the turbulent kinetic energy, E^S, is thus also obtained.

Figure 3a shows time-averaged plots of the turbulent kinetic energy spectra E^S based on spatial FFT analysis of data sets for 40 successive times separated by a time interval $0.1/f$, at the intermediate resolution (with the cell size 1.5Δ) and on 110^3 downstream grid subvolumes chosen as in Fig. 2a. The largest wavenumber for which spectral amplitudes are plotted corresponds to a wavelength of four computational cells, and normalization of $k = |\mathbf{k}|$ is such that $k = 1$ corresponds to the length scale D_e. Figure 3a shows short simulated inertial subranges for k approximately between $1 < k < 2.5$, consistent with the $k^{-5/3}$ inviscid subrange of the Kolmogorov K41 theory, and suggesting (Fig. 3b) the experimentally observed shallower slope (than $k^{-5/3}$) in the near-dissipation region (e.g., [60]). The inertial subrange is followed by faster decay of amplitudes due to the effective self-similar MILES dissipation [23, 49].

Based on the energy spectra $E(k)$ we can obtain useful quantitative statistical measurements (cf. Table II) for the resolved integral scale λ_1, the characteristic rms velocity fluctuations u', and the characteristic rms vorticity ω' within the downstream subvolumes.

TABLE II
Statistical Jet Measures[a]

AR	u'/U_j	$\omega' D_e/U_j$	L_1/D_e
1	0.26 (0.22)	3.7 (3.2)	0.33 (0.32)
2	0.25 (0.21)	3.6 (3.1)	0.33 (0.32)
3	0.29 (0.25)	4.1 (3.5)	0.35 (0.34)

[a] Values in parentheses were evaluated using the solenoidal velocity component.

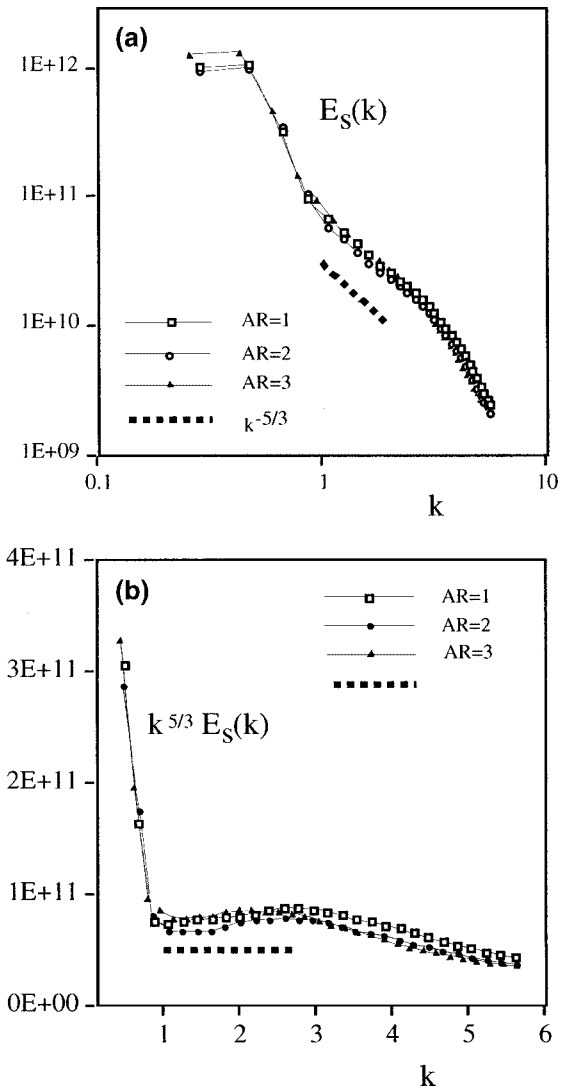

FIG. 3. (a) Downstream turbulent kinetic energy spectra $E^s(k)$ for rectangular jets as a function of aspect ratio AR. (b) Compensated spectra $k^{5/3}E^s(k)$.

More precisely, we can evaluate $u'^2 = \frac{2}{3}\int E(|\mathbf{k}|)\,d|\mathbf{k}|$, $\omega'^2 = 2\int |\mathbf{k}|^2 E(|\mathbf{k}|)\,d|\mathbf{k}|$, and $\lambda_1 = \pi/2\int |\mathbf{k}|^{-1}E(|\mathbf{k}|)\,d|\mathbf{k}|/u'^2$, with integrations restricted to the simulated inertial subrange (Fig. 3). Measures based only on E^S are also shown between parentheses in Table II; Table II indicates fairly similar jet velocity fluctuation levels features for AR = 1 and 2 and significantly higher for AR = 3; the consistently larger turbulence fluctuation levels for AR = 3 are in agreement with the AR-dependent vorticity geometry and streamwise vorticity production discussed above and elsewhere [56]. The possible dependence of the resolved small-scale jet features discussed above on the specifics of the SGS modeling are assessed in what follows, based on the raw Euler and NS equations with and without SMG viscosity. Analysis is based on the instantaneous jet velocity data on 90^3 grid subvolumes, including only appropriate downstream portions of the jets chosen similarly around the

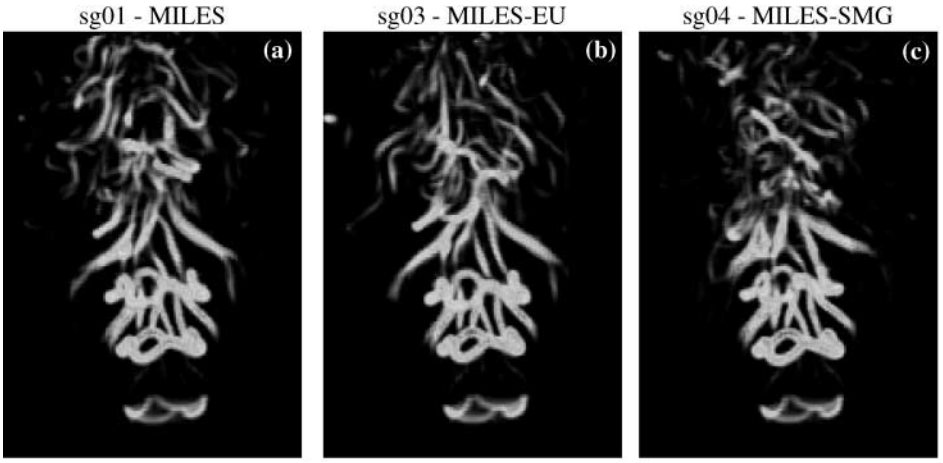

FIG. 4. Instantaneous flow visualizations of square jets simulated with MILES, MILES-EU, and MILES-SMG (same times and color mappings chosen).

jet centerline, as described above (Fig. 2a). The simulations discussed in connection with Figs. 4–6 were performed using the intermediate-resolution grid (cell size 1.5Δ in Table I) with identical initial conditions.

The virtually identical λ_2 distributions in the lower half of the frames in Fig. 4 correspond to the initial larger scale vortex dynamics; globally similar but distinctly different local features are apparent as we move farther downstream, as the flow regime becomes disorganized and dominated by the presence of thin elongated vortices. Figure 5 shows very similar velocity-fluctuation spectra for all three MILES approaches, indicating (i) somewhat smaller amplitudes for lower wavenumbers associated with MILES and MILES-SMG, depicting

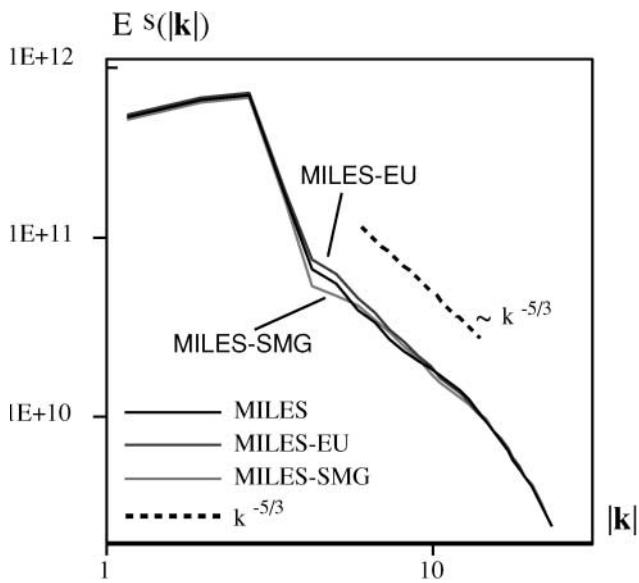

FIG. 5. Downstream turbulent kinetic energy spectra $E^s(k)$ for the square jets shown in Fig. 4.

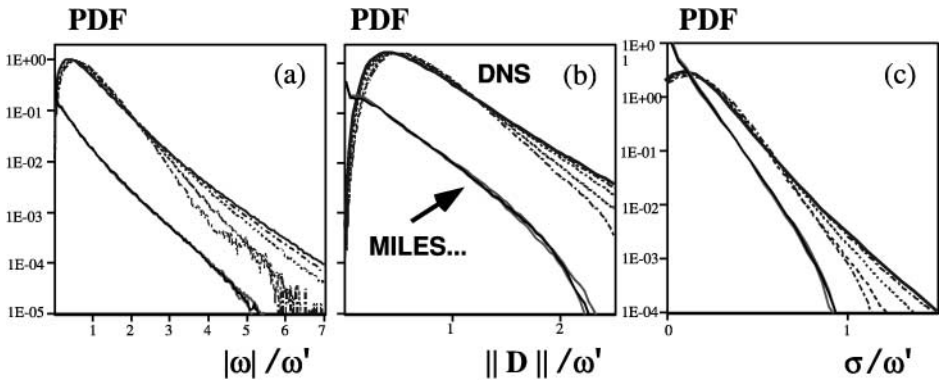

FIG. 6. PDFs of the vorticity magnitude (a), strain rate magnitude (b), and stretching (c) based on the downstream subvolume data for the square jets shown in Fig. 4, compared to that of DNS of homogeneous turbulence (cf., [9]). Plot legends are the same as in Fig. 7.

viscous damping of resolved GS features; (ii) essentially coincident high-wavenumber amplitudes—reflecting the unresolved small-scale viscous effects; (iii) captured inertial subrange. The structure of the resolved vorticity implies that high-intensity regions tend to be organized generally in elongated tubes. Worm vortices usually involve fractional volumes of order 1% or less [23], consistent with the results of Jimenez *et al.* [9] based on DNS of homogeneous isotropic turbulence.

The distribution of vorticity magnitude $|\omega|$, rate of strain $\|\mathbf{D}\|$, and stretching $\sigma = (\omega \cdot \mathbf{D}\omega)/|\omega|^2$ can be examined based on the corresponding time-averaged PDFs shown in Fig. 6, which are compared with the DNS data of Jimenez *et al.* [9] for incompressible forced homogeneous isotropic turbulence. For each subvolume data a characteristic vorticity scale ω' is defined and evaluated using the solenoidal velocity component, as previously discussed.

As discussed in Fureby and Grinstein [23], a major difference between the jet data considered here and homogeneous turbulence data relates to the behavior of the PDFs of the vorticity magnitude for small values of $|\omega|$ (Fig. 6a). Because of the transitional and nonhomogeneous nature of the jet regime (e.g., the jet core and surroundings consist mainly of irrotational or nearly irrotational fluid), probabilities of occurrence of small values of, say, $|\omega| < 0.5$ appear as the largest when based on jet data—in contrast to smaller probabilities there based on analysis of the developed homogenous turbulence data. We can argue along the same lines to explain the similar differences in the distributions for small values of strain rate and stretching between MILES of transitional jets and DNS of homogeneous turbulence (cf. Figs. 6b and 6c), which also reflect more significantly on the specially anisotropic features of the jet flow (e.g., as indicated by the streamwise velocity distributions in Fig. 4a). Otherwise, PDFs based on both transitional jet flows and homogeneous turbulence show similar monotonically decreasing trends for the "larger" values. Based on the vorticity data, for which the comparison between jet and box data appears more meaningful, we can renormalize the jet PDFs to improve on these comparisons quantitatively by requiring that jet and box data PDFs coincide with the corresponding PDFs of the box data at the intermediate crossover value $|\omega| \approx 2.2$, for which the DNS-based PDFs appear to be fairly Re independent (Fig. 7). For the grid resolution used, the best viual fit of MILES vorticity PDF with DNS data in Fig. 6 suggests an effective $\mathrm{Re}_{\mathcal{T}} < 94$ for the jet data.

5.3. *Fully Developed Turbulent Channel Flow*

Next we focus on fully developed wall-bounded flows in a channel confined between two parallel plates at a distance $2h$ apart, where h is the channel half-width. The flow is driven by a constant mass flow in the streamwise ($\mathbf{e}_1$) direction defining the mean velocity $\langle\bar{\mathbf{v}}\rangle$. No-slip conditions are enforced in the cross-stream ($\mathbf{e}_2$) direction and periodic conditions are applied in the spanwise ($\mathbf{e}_3$) direction. As initial conditions we use a parabolic velocity profile, to which finite amplitude perturbations with a 5% peak amplitude are superimposed. After the simulations reached a statistically steady state they were continued for another $40h/u_\tau$ time units to obtain statistics, where $u_\tau = \tau_w^{1/2}$ is the friction velocity and τ_w the evaluated wall-shear stress. We considered two cases, with target friction velocity based Re numbers $\mathrm{Re}_\tau = 395$ and 2030, for which reference data is available from virtually identical DNS data sets [61, 62] and laboratory experiments [63], respectively. The size of the channel is $6h \times 2h \times 3h$ in the streamwise, cross-stream, and spanwise directions. In order to study the effects of resolution two grids of 90^3 and 60^3 cells were employed, having uniform spacing in the $\mathbf{e}_1$ and $\mathbf{e}_3$ directions while geometrical progression was used in the $\mathbf{e}_2$ direction to concentrate the grid toward the walls, with the first cell at between $y^+ \approx 1$ and 10. The nondimensionalized cell spacing is $\Delta x_1^+ \approx 20$–40 and $\Delta x_3^+ \approx 10$–20 for the $\mathrm{Re}_\tau = 395$, and $\Delta x_1^+ \approx 100$–200 and $\Delta x_3^+ \approx 60$–100 for the $\mathrm{Re}_\tau = 2030$ case.

The code solves the discretized governing Eqs. (4) and (5) or (8) and (9), depending on whether conventional LES or MILES are used, based on decoupling the pressure–velocity system by combining the continuity and momentum equations. This is accomplished by inserting the face interpolate F_f^ρ, as obtained directly from the momentum equation, into the continuity equation, and the resulting equation takes the form of a Poisson equation for the pressure. The equations are integrated in time using the second-order-accurate three-point backward difference scheme, with $m = 2, \alpha_0 = \frac{1}{2}, \alpha_1 = -2, \alpha_2 = \frac{3}{2}, \beta_0 = \beta_1 = 0$, and $\beta_2 = 1$. The scalar equations are solved sequentially, with iteration over the explicit coupling terms to obtain rapid convergence. The segregated approach results in a Courant (Co) number restriction; a maximum Co number of 0.5 gives satisfactory numerical stability and temporal accuracy, but a value of $\mathrm{Co} \approx 0.2$ is preferable since LES attempts to resolve and capture the dynamics of resolvable eddies and large coherent structures.

In Table III the global parameters of the channel flow simulations are listed; following standard practice $U_m = \frac{1}{2}\int_{-1}^{1}(\bar{v}_1)\, d(\frac{x_2}{\delta})$ is the bulk velocity, $\mathrm{Re}_\tau = u_\tau \delta/\nu$ is the

TABLE III
Nominal Characteristic Parameters for the Channel Flow Simulations

	Grid	Re_τ	U_C/U_m	U_m/u_τ	C_f	$\Delta\ell_3^+$	Numerics
DNS [61]	160×256^2	395	1.14	17.47	$6.55\mathrm{e}^{-03}$	100	$O(\Delta t^2$, spectral)
LES-SMG	60^3 (90^3)	384 (393)	1.12 (1.13)	17.1 (17.2)	$6.2\mathrm{e}^{-03}$ ($6.6\mathrm{e}^{-03}$)	121 (117)	$O(\Delta t^2, \mathbf{d}^2)$
LES-DSMG	60^3 (90^3)	398 (397)	1.14 (1.14)	17.6 (17.4)	$6.7\mathrm{e}^{-03}$ ($6.5\mathrm{e}^{-03}$)	117 (119)	$O(\Delta t^2, \mathbf{d}^2)$
LES-DSM	60^3 (90^3)	389 (397)	1.15 (1.14)	17.2 (17.3)	$6.4\mathrm{e}^{-03}$ ($6.5\mathrm{e}^{-03}$)	104 (103)	$O(\Delta t^2, \mathbf{d}^2)$
MILES	60^3 (90^3)	390 (394)	1.13 (1.14)	17.4 (17.7)	$6.4\mathrm{e}^{-03}$ ($6.6\mathrm{e}^{-03}$)	110 (105)	$O(\Delta t^2, \mathbf{d}^2)$ + FCT
EXP [63]		2030					
LES-SMG	60^3 (90^3)	2026 (2041)	1.07 (1.10)	18.3 (18.7)	$4.3\mathrm{e}^{-03}$ ($4.6\mathrm{e}^{-03}$)	249 (156)	$O(\Delta t^2, \mathbf{d}^2)$
LES-DSMG	60^3 (90^3)	2031 (2040)	1.09 (1.8)	18.4 (18.6)	$4.4\mathrm{e}^{-03}$ ($4.8\mathrm{e}^{-03}$)	243 (138)	$O(\Delta t^2, \mathbf{d}^2)$
LES-DSM	60^3 (90^3)	2034 (2042)	1.08 (1.9)	18.5 (18.9)	$4.5\mathrm{e}^{-03}$ ($4.8\mathrm{e}^{-03}$)	214 (127)	$O(\Delta t^2, \mathbf{d}^2)$
MILES	60^3 (90^3)	2048 (2036)	1.10 (1.9)	18.4 (18.8)	$4.6\mathrm{e}^{-03}$ ($4.9\mathrm{e}^{-03}$)	225 (146)	$O(\Delta t^2, \mathbf{d}^2)$ + FCT

friction-velocity Reynolds number, and $C_f = \tau_w / \frac{1}{2}\bar{\rho} U_m^2$ is the mean skin-friction coefficient. These are all in acceptable agreement with DNS and experimental data. However, when comparing LES and MILES predictions, differences are observed with respect to spatial resolution at a given Re_τ number, and with respect to Re_τ number effects, at a given resolution. The influence of the (explicit or implicit) SGS model on the global parameters is comparatively small, with DSM giving the best agreement, independent of grid spacing. Comparing the computed mean streak spacing $\Delta\ell_3^+$ gives a first indication of the predictive capabilities of the LES models. At $\mathrm{Re}_\tau = 395$ the mean streak spacing is resolved, and all LES models give predictions within 20% of the DNS data (which is to be considered reasonable), with DSM giving the best agreement. At $\mathrm{Re}_\tau = 2030$ the mean streak spacing is not resolved on any of the grids, and the predicted mean streak spacing is found to be between $2.0\Delta x_3^+$ and $2.5\Delta x_3^+$. This distance may thus be representative of the smallest coherent structure that can be resolved. Comparing statistical properties from the simulations with the experimental correlations of Dean [64], e.g., $U_C / U_m \approx 1.28 \cdot \mathrm{Re}_m^{-0.016}$ and $C_f \approx 0.073 \cdot \mathrm{Re}_m^{-0.25}$, where U_C is the mean centerline velocity and $\mathrm{Re}_m = U_m 2\delta/\nu$, shows good agreement, supporting the ability of LES and MILES to capture the global effects associated with Re-number variations—even though $\Delta\ell_3^+$ is not properly resolved at $\mathrm{Re}_\tau = 2030$.

In Fig. 8 the outstanding flow features in the lower half of the channel are presented in terms of vortex lines, contours of the streamwise vorticity on side and bottom walls, and an isosurface of the second invariant of the velocity gradient $Q = \frac{1}{2}(\|\mathbf{W}\|^2 - \|\mathbf{D}\|^2)$. In Figs. 8a–8c we show results from $\mathrm{Re}_\tau = 395$ using MILES, SMG, and DSMG at 60^3 resolution, and in Fig. 8d we show results from $\mathrm{Re}_\tau = 2030$ using MILES at 90^3 resolution. The location of a vortex line is given by the equation $d\mathbf{x}/ds = \boldsymbol{\omega}/|\bar{\omega}|$, where s is the distance along the vortex line. This equation is integrated for $\mathbf{x}$ using a second-order Runge–Kutta method, and second-order linear interpolation is used to compute the vorticity from the grid points. Based on instantaneous flow visualizations it is virtually impossible to distinguish between predictions from individual (explicit or implicit) SGS models. The most noticeable feature in Fig. 8 is the difference in size of CSs in the wall proximity, associated with different Re_τ numbers. In wall units, however, sizes are virtually identical for a given Re_τ, the radius of the CS is about 20δ, the length is about 1000δ, and the distance from the wall is between 20δ and 30δ. By correlating isosurfaces of Q with the velocity it is found that vortices located above the low-speed streaks are repeatedly ejected away from the wall, as formerly found in both experiments and DNS/LES studies, which produces hairpin vortices stretched by the ambient shear, as illustrated with vortex lines in Fig. 8. It is through this ejection mechanism that vorticity, produced in the vicinity of the wall, is advected into the boundary layer, making it turbulent. An interesting observation, also found in DNS, is that the hairpins are asymmetric, with one leg (usually the right leg) considerably stronger than the other. Although various models based on experiments or simulations have been proposed [65, 66], the interpretation of low- and high-speed streaks and their relation with the ejection mechanism are still not fully understood.

Figure 9 shows the mean-velocity profiles $\langle \bar{v}_1 \rangle$ for the cases reported in Table III, where $\langle \cdot \rangle$ denotes combined spanwise, streamwise, and time averaging. The $\langle \bar{v}_1 \rangle$ profiles are in good agreement with each other as well as with the DNS [61, 62] and experimental data [63] used as reference. The differences in the centerline velocity U_C apparent in Fig. 9a reflect on differences between forcing mechanisms involved in the DNS and present simulations. This, however, does not influence the statistics and the near-wall behavior, since the ratios U_C / u_τ

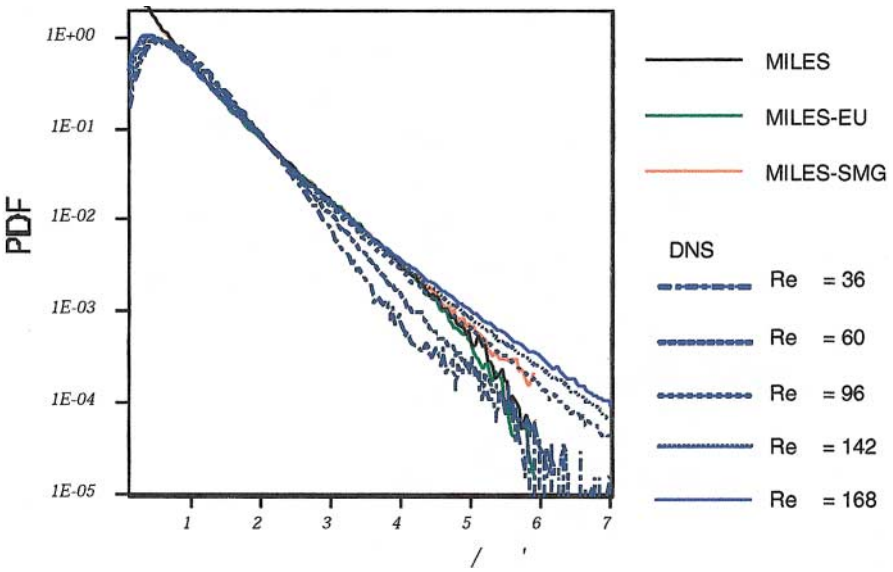

FIG. 7. Renormalized PDF of the vorticity magnitude based on the downstream subvolume data for the square jets shown in Fig. 5, compared to that of DNS of homogeneous turbulence (cf., [9]).

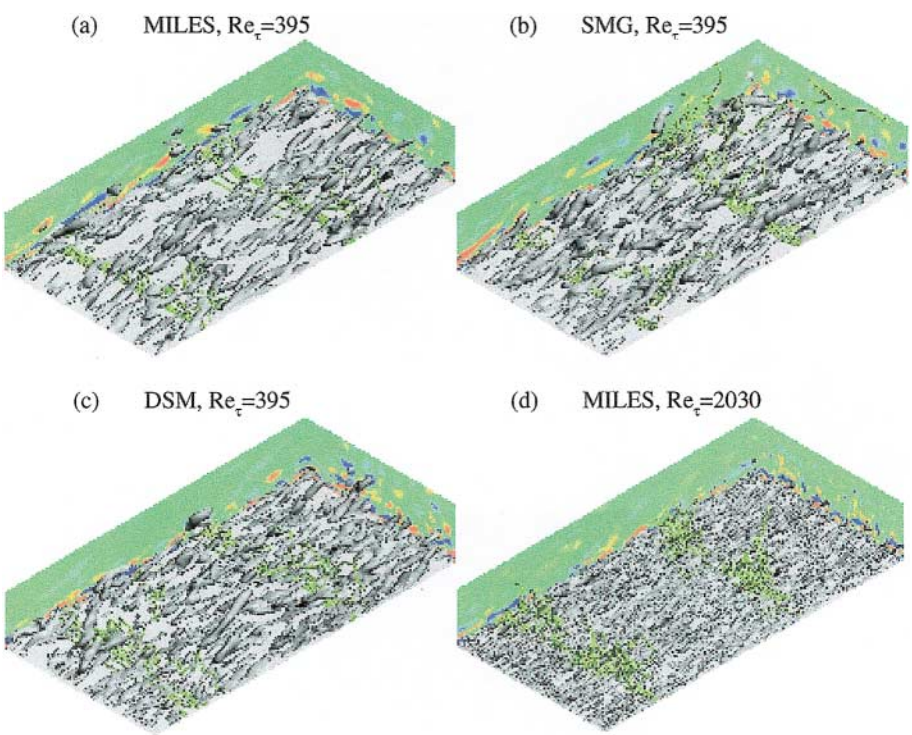

FIG. 8. Contours of streamwise vorticity projected onto side and bottom walls, vortex lines, and iso-surfaces for $Q = 1$ for (a) MILES, (b) SMG, and (c) DSM at $\mathrm{Re}_\tau = 395$ and for (d) MILES at $\mathrm{Re}_\tau = 2030$.

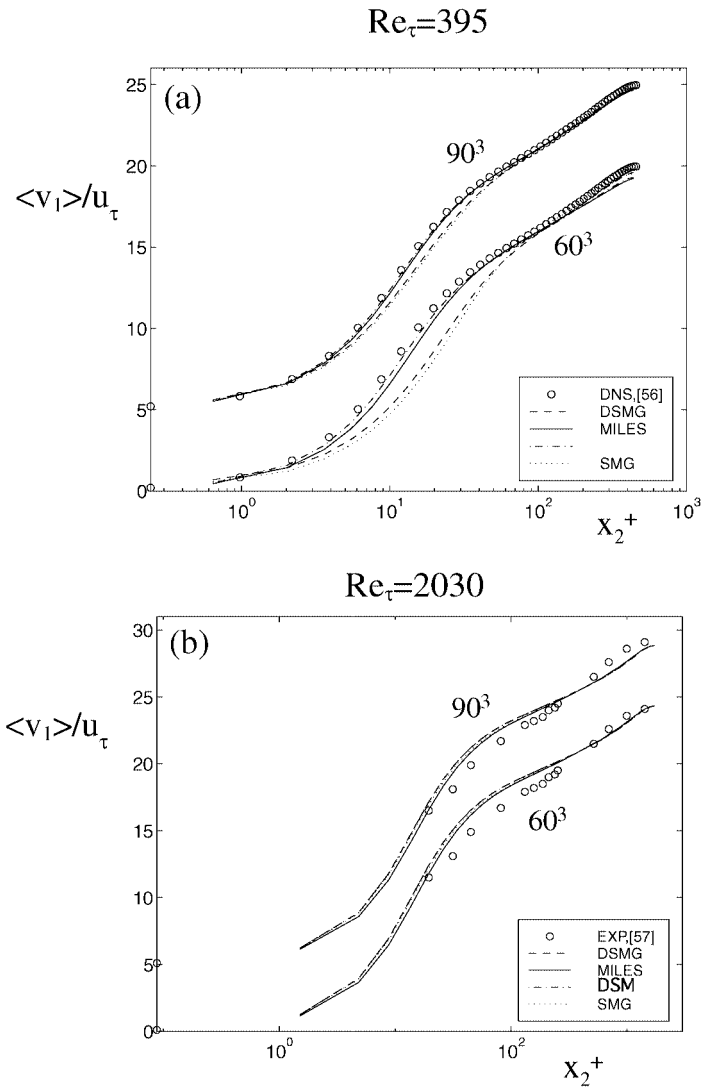

FIG. 9. Mean-velocity profiles $\langle \bar{v}_1 \rangle$for the channel flow cases reported in Table III. The 90^3 results have been shifted by 5 units in the vertical direction to improve visualization.

and U_m/u_τ are unaffected. For $\mathrm{Re}_\tau = 395$, differences attributed to gridding are small and are mainly limited to the buffer region ($5 < x_2^+ < 50$), suggesting that the 60^3 resolution is sufficient. However, for $\mathrm{Re}_\tau = 2030$ differences due to gridding are more noticeable and can also be observed in the viscous sublayer ($x_2^+ < 5$), in the buffer layer ($5 < x_2^+ < 50$), and in the logarithmic layer ($50 < x_2^+ < 200$), suggesting that at least 90^3 resolution is required. Differences in $\langle \bar{v}_1 \rangle$ due to SGS models are generally minor and limited to the region $x_2^+ < 90$. However, DSM and MILES both appear to give improved predictions of $\langle \bar{v}_1 \rangle$ in the wall proximity compared to SGS models derived under the assumption of alignment between the deviatoric part of $\mathbf{B}$ and the deviatoric part of $\bar{\mathbf{D}}$. Discordant with contemporary LES [68], DSMG appears not to significantly improve these predictions. In addition, it

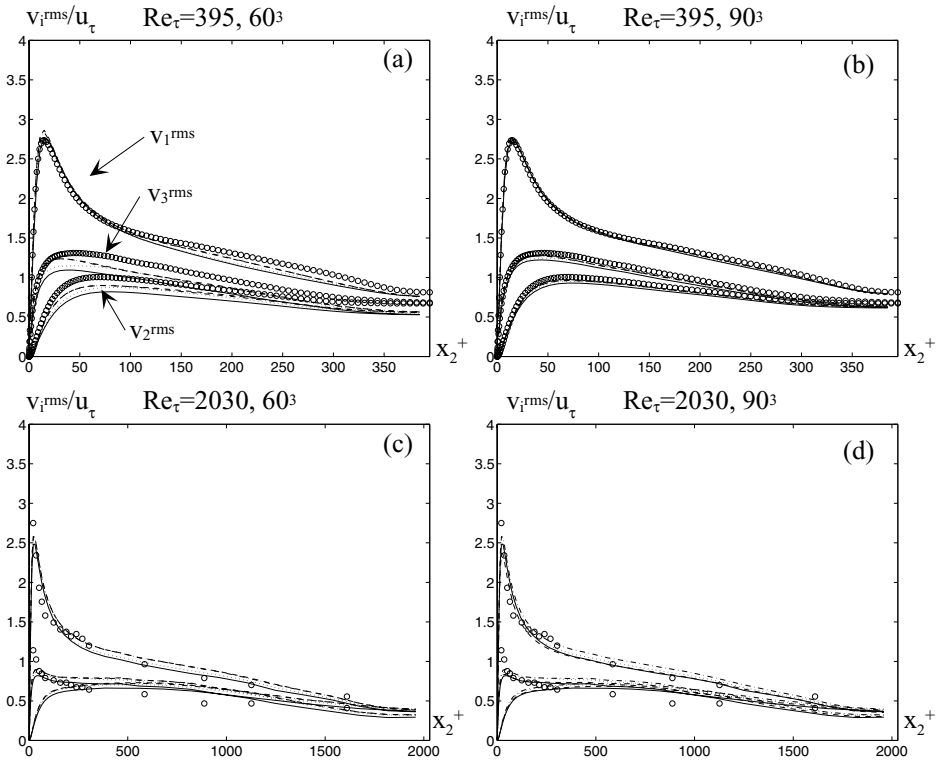

FIG. 10. Rms velocity fluctuation profiles $v_i^{\rm rms} = \sqrt{\langle(\bar{v}_i - \langle\bar{v}_i\rangle)^2\rangle}$, $i = 1$–3, for the channel flow cases listed in Table III. Legends as in Fig. 9.

seems that at least for the computational grids used in this study, the law of the wall and the corresponding logarithmic layer and von Kármán constant can be retrieved with virtually no dependence on the grid topology and resolution. A curve fit for the logarithmic region yields $U^+ = A + (1/\kappa)\ln x_2^+$, with the coefficients $A \approx 5.1 \pm 0.2$ and $\kappa \approx 0.41 \pm 0.04$, respectively, with the largest difference obtained when using SMG. Such a good agreement with DNS and experimental data is particularly significant in light of the fact that the particular length scale of both the explicit and implicit SGS models is a function of the grid spacing.

Figure 10 shows the corresponding rms velocity fluctuation profiles $v_i^{\rm rms} = \sqrt{\langle(\bar{v}_i - \langle\bar{v}_i\rangle)^2}$, $i = 1$–3. For the $\mathrm{Re}_\tau = 395$ case the overall agreement of the predicted rms velocity fluctuations with the DNS data is good. However, the influence of spatial resolution is significant, in particular for $v_1^{\rm rms}$ at $\mathrm{Re}_\tau = 395$ at $y^+ > 150$ and for $v_2^{\rm rms}$ and $v_3^{\rm rms}$ across the full channel width. For $\mathrm{Re}_\tau = 2030$ this problem should be accentuated but it appears only to be important at $y^+ < 50$. The differences in statistics due to (explicit or implicit) SGS models can also be seen—in particular for $v_2^{\rm rms}$ and $v_3^{\rm rms}$. MILES and DSM give virtually identical profiles, overpredicting peak values of $v_1^{\rm rms}$ by about 8% on the 60^3 grid and 5% on the 90^3 grid, while underpredicting the profiles of $v_2^{\rm rms}$ and $v_3^{\rm rms}$ by 10% on the 60^3 grid and 5% on the 90^3 grid. SMG underpredicts the peak value of $v_1^{\rm rms}$ by approximately 7% and the profiles

of v_2^{rms} and v_3^{rms} by 15% on the 60^3 grid and 5% on the 90^3 grid. Moreover, DSMG shows only minor improvements over SMG for the rms velocity fluctuations at $\text{Re}_\tau = 395$. For the $\text{Re}_\tau = 2030$ case the differences are larger between the statistics obtained from the 60^3 grid than those from the 90^3 grid, and moreover, the differences between the SGS models are also more pronounced on the 60^3 grid. In particular, the MILES and DSM models still show the smallest deviations from the reference data [61] on the fine grid, with MILES showing the largest deviation at the coarse grid. DSMG and SMG both underpredict the peak value of v_1^{rms} and the profiles of v_2^{rms} and v_3^{rms} within 10–15%. The position of the peak v_1^{rms} ($x_2^+ \approx 15$–25) is in reasonable agreement with measurements and DNS data (i.e., $x_2^+ \approx 12$–20), while the LES of Moin and Kim [68] report larger differences at $\text{Re}_\tau = 640$ ($x_2^+ \approx 30$). The v_2^{rms} and v_3^{rms} profiles from SMG and DSMG are flatter than the DNS data and the profiles from MILES and DSM, suggesting DSM and MILES may deal with anisotropy effects better than SMG and DSM because of their tensorial properties.

Figure 11 shows resolvable Reynolds stress profiles $-\langle v_1' v_2' \rangle$ and total Reynolds stress profiles $-\langle v_1' v_2' \rangle + \langle B_{12} \rangle$, where $v_i' = \bar{v}_i - \langle \bar{v}_i \rangle$ denotes the resolvable velocity fluctuations for all cases reported in Table III. Based on evaluations of the shear stress $-\langle v_1' v_2' \rangle + (1/\text{Re}_\tau)(\partial \langle \bar{v}_2 \rangle / \partial x_2)$, it is clear that the flow is in equilibrium, with the total shear stress balancing the

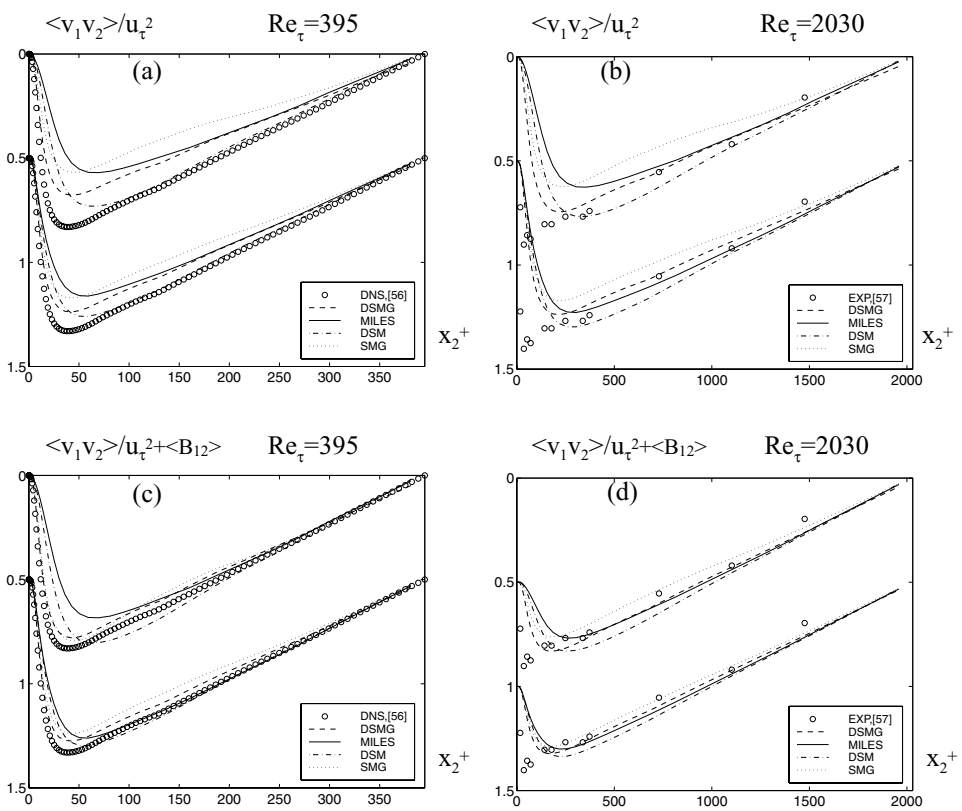

FIG. 11. Resolvable Reynolds stress profiles $\langle v_1' v_2' \rangle$ at (a) $\text{Re}_\tau = 395$ and (b) $\text{Re}_\tau = 2030$, and effective Reynolds stress profiles $\langle v_1' v_2' \rangle + \langle B_{12} \rangle$ at (c) $\text{Re}_\tau = 395$ and (d) $\text{Re}_\tau = 2030$ for all channel flow cases reported in Table III. The 90^3 results are shifted (downward) by 0.5 units in the vertical direction to improve visualization.

downstream mean pressure gradient in the regions away from the walls. The contribution of the (explicit) SGS model is negligible far from the walls; however, in the viscous sublayer and in the buffer layer, the SGS contribution is comparatively large and differences between SGS models are found. In general, the (explicit or implicit) SGS models tend to increase the effective shear stress in the wall proximity relative to the reference. For both Re_τ numbers the best overall agreement with experimental or DNS data is obtained with DSM closely followed by MILES, DSMG, and SMG. The difference between the results is small (about 10%) and may be attributed to both the average effect of the SGS model, i.e., $\langle B_{12}\rangle$, and the resolvable part $-\langle v_1' v_2'\rangle$ that is implicitly affected by $\mathbf{B}$. In the $\mathrm{Re}_\tau = 2030$ case, spatial resolution is inadequate to resolve the mean streak spacing and hence much of the dynamics of the flow in the near-wall region is not well captured. This manifests itself in the rather poor predictions of the resolvable shear stresses $-\langle v_1' v_2'\rangle$ (Fig. 11b). The SGS model is thus required to capture an increasing fraction of the shear stress (and other statistical quantities)—which some models do better than other models (Fig. 11d); the rather poor agreement noted here indicates that improved estimates of the SGS flow physics—and thus improved SGS modeling—are required. Finally, it is worth noting that the maxima of the total shear stress $\langle v_1' v_2'\rangle + \langle B_{12}\rangle$ increase in magnitude and are closer to the wall as Re_τ increases. Since the peak value of $\langle v_1' v_2'\rangle + \langle B_{12}\rangle$ is not the same for each profile, it does not scale properly with the inner variables (i.e., $(\langle v_1' v_2'\rangle + \langle B_{12}\rangle)/u_\tau^2$ and y^+) in the Re_τ-number range examined (see also the experimental results of Wei and Willmarth [63] and Comte-Bellot [69]).

Figure 12 shows instantaneous contour plots of the effective (explicit or implicit) SGS eddy viscosity at the midplane of the channel from LES using (a) SMG, (b) DSM, and (c) MILES at $\mathrm{Re}_\tau = 395$ and (d) DSM at $\mathrm{Re}_\tau = 2030$. The representative (explicit or implicit) SGS eddy viscosity ν^* is defined from $\nu^* = \frac{1}{2}\mathbf{B}\cdot\bar{\mathbf{D}}/\|\bar{\mathbf{D}}\|^2$ or $\nu^* = \frac{1}{2}\mathbf{B}\cdot\bar{\mathbf{D}}/\|\bar{\mathbf{D}}\|^2$, which implies that $\nu^* = \nu_k$ for all eddy-viscosity models. By comparing Figs. 12a and 12c we see that peak value of ν^* is virtually identical between SMG and MILES and is reduced by a factor of two for DSM. However, the distributions of ν^* are quite different: for DSM the distribution is fairly even, while for both SMG and MILES the distributions are quite irregular, with alternating peaks and regions of virtually zero ν^* and with MILES also exhibiting very low values of ν^* in the core region. Comparing integrated profiles of ν^* across the spanwise and streamwise extent of the channel confirms the first impression, that MILES results in the lowest amount of ν^* while SMG results in the highest. The value of ν^* vanishes as the wall is approached for all SGS models: for SMG this is due to variation of ν^* with Re_Δ, for DSM this is due to the boundary conditions applied to $\mathbf{B}$, i.e., $\mathbf{B} = \mathbf{0}$ at the wall and the built-in relaxation, and for MILES this is due to the behavior of the flux limiter in conjunction with how the spatial resolution affects the velocity and its gradient. If $\mathbf{v} = \mathbf{0}$ on the wall, the definition of $\mathbf{B}$ implies that only the rapid part $\mathbf{B}^{(2)} = \beta(\Gamma)\mathbf{Ld}\otimes\mathbf{Ld}$ remains, which is characteristic of nonequilibrium flows or of regions where Δ is not very small compared to λ_l, which approaches λ_K or zero. Thus, the flux limiter Γ accommodates the automatic relaxation of $\mathbf{B}$ to $\mathbf{0}$ on the wall. In the wall proximity, i.e., in the boundary layer, the local and instantaneous state of the flow determine the balance between the rapid and slow parts of $\mathbf{B}$ using information of the resolved flow via the flux limiter Γ. Investigation of the effects of using different types of flux limiters on the simulated near-wall statistics and flow topology is thus extremely important and deserves to be taken further.

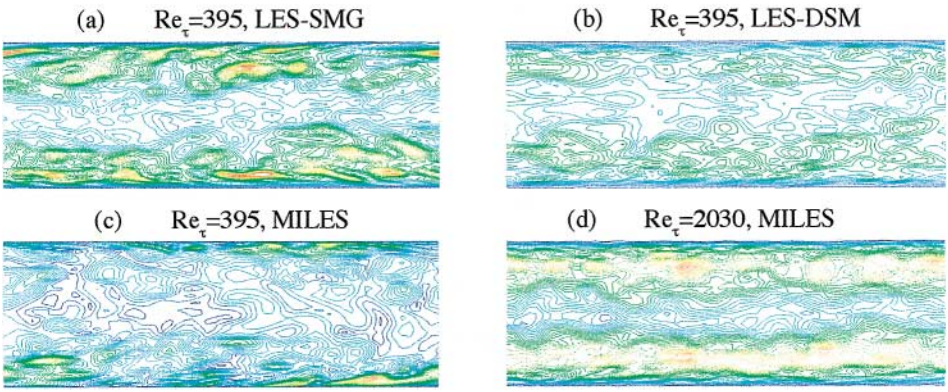

FIG. 12. Instantaneous iso-contours of the effective scalar valued SGS viscosity for (a) SMG, (b) DSM, and (c) MILES at $\mathrm{Re}_\tau = 395$ and for (d) DSM at $\mathrm{Re}_\tau = 2030$. Contour levels are the same for each figure and span the range between $\nu^*/\nu = 1$ (blue) and $\nu^*/\nu = 4$ (red) for $\mathrm{Re}_\tau = 395$ and $\nu^*/\nu = 1$ (blue) and $\nu^*/\nu = 13$ (red) for $\mathrm{Re}_\tau = 2030$.

6. CONCLUDING REMARKS

In conventional LES, explicit SGS models are introduced explicitly for closure and to provide a mechanism by which dissipation of kinetic energy accumulated at high wavenumbers may occur. Applications involving inhomogeneous turbulent flows typically demand improved SGS modeling capable of capturing the inherently anisotropic small-scale flow features. The MILES approach provides a promising practical alternative to conventional LES, involving the solution of the unfiltered NSE with high-resolution locally monotone algorithms by which the effects of the SGS flow physics on the GS flow are incorporated into the functional reconstruction of the convective fluxes. A formal advantage of MILES is that no commutation errors are involved, since it uses no explicit filtering; this may or may not be of practical consequence, since commutation errors can be lumped together with the explicit subgrid models. Because of the intrinsically anisotropic nature of the SGS modeling in MILES associated with the functional reconstruction, with possibilities of simultaneously handling flow and grid anisotropies, we expect it may provide an optimal computational framework for inhomogeneous high-Re flows.

The main goals of the present study have been to improve our understanding of the formal properties of the effective SGS modeling of MILES using the modified equations' formalism, and to further document the properties of MILES using databases from simulations; homogeneous turbulence decay and both free and wall-bounded inhomogeneous flows have been investigated in this context.

Although the history of MILES draws on analogies with the development of shock-capture schemes, the concept of MILES, as developed here and in our earlier work [23], attempts to embody a general computational procedure for solving the NSE for high-Re-number turbulent flows as accurately as possible using built-in, or implicit, SGS models. We have chosen to emphasize the overall modeling aspects of LES based on the modified equations, which are seldom examined in this context. Analysis based on the modified equations can be used to examine how explicit SGS model terms compete with leading-order truncation errors resulting from discretization. Likewise, the analysis can be also used to address the extent to which the leading-order truncation may provide an SGS model implicitly

when suitable computational algorithms are used. It is worth reiterating here that relying on arbitrary methods to emulate the additional required damping to achieve numerical stability will not necessarily provide the smooth transition to SGSs ensuring the correct distribution of energy on the GSs in general. We have used the modified equations' analysis to show that a particular form of functional reconstruction—involving flux limiters—can be consistently regarded as an implicitly implemented LES approach, where choosing flux limiters is effectively similar to choosing an SGS model in conventional LES.

We can envision extending MILES to the more general concept of *integrated* LES (ILES), in which the functional reconstruction of the convective terms is carried out using high-resolution flux-limiting methods, and where the leading-order truncation error of the modified equations acts as an implicit SGS model. However, the implicit SGS model must be able to mimic the SGS turbulence in terms of accurate inertial subrange and near-wall behaviors and we anticipate that only a few such reconstruction schemes will fulfill these requirements. In particular, further study is required to extend the present analysis to include other types of flux limiters, e.g., such as is effectively used with locally monotonic PPM [11], or with locally nonmonotonic approaches involving a third-order upwind-biased convection algorithm (e.g., [70]). Beyond the academic interest of performing such extensions to further develop our understanding of ILES, the practical challenge is to identify the suitable features which should be built into the flux limiters—and thus into the numerical schemes—to achieve desirable physical properties in the associated implicit SGS modeling.

The results from the decaying isotropic turbulence case show that the decay rate of the energy spectra can be predicted equally well using MILES or explicit (SMG, DSM) SGS models; improved resolution has the effect of extending the captured portion of the inertial subrange in similar ways for all models. Comparison of MILES of transitional free jets initialized with identical laminar conditions, based on the Euler equations (MILES-EU) and on the NSE with (MILES-SMG) or without (MILES) Smagorinsky viscosity, showed very similar results and good agreement with DNS of homogeneous turbulence on their downstream transitional regions, including (i) captured inertial subrange and simulated self-similar dissipation regions within the velocity spectra, and (ii) nearly identical CDFs of the vorticity magnitude—which becomes virtually independent of the specific implicit SGS model when adequate spatiotemporal resolution is involved.

Our previous comparisons between MILES and conventional LES for high-Re free shear flows [23] indicated that MILES is generally not worse than conventional LES and suggested that once the cutoff wavenumber lies within the inertial subrange, MILES tends to compare favorably for higher Re and/or improved resolution. These trends have been also confirmed for the wall-bounded (channel) flows investigated in the present work. Because in applications involving turbulent flows near walls for fewer universal properties are involved and characteristic length scales of the most energetic eddies decrease, SGS models capable of handling simultaneous flow and grid anisotropy, such as is built into the MILES approach, can be reasonably expected to provide an efficient computational procedure in this context. We have demonstrated that MILES reproduces the first- and second-order statistical moments of the velocity field almost as accurately as the DSM and better than isotropic eddy-viscosity models. MILES is also very competitive computationally. Typical comparative work figures on the channel flow simulations were the following: SMG $= 1$, MILES $= 0.95$, DSMG $= 1.2$, DSM $= 1.6$. We argue that this is due to the intrinsic nature of the MILES model, in which a nonlinear tensorial eddy-viscosity model is built into the algorithm based on a carefully chosen functional reconstruction of the convective terms.

For completeness, we note recent related papers reporting use of TVD-based schemes as flux-limiting-based implicitly implemented SGS models [71], PPM-based studies of homogeneous turbulence [72], studies of channel flows using Godunov's exact Riemann solver [73], and applications of the spectral vanishing viscosity method [74], combining concepts of monotonicity and LES in nonlinear conservation laws.

ACKNOWLEDGMENTS

A critical reading by Philippe Spalart of an early version of the paper is greatly appreciated. This research is performed with support from ONR through the NRL 6.1 Computational Physics task area and computer time is provided by the DoD-HPC-MP program.

REFERENCES

1. M. Lesieur and O. Metais, New trends in large eddy simulations of turbulence, *Annu. Rev. Fluid Mech.* **28**, 45 (1996).
2. U. Frisch, *Turbulence* (Cambridge Univ. Press, Cambridge, UK, 1995).
3. S. Ghosal and P. Moin, The basic equations for the large eddy simulation of turbulent flows in complex geometry, *J. Comp. Phys.* **118**, 24 (1995).
4. C. Fureby and G. Tabor, Mathematical and physical constraints of large eddy simulations, *J. Theor. Comp. Fluid Dyn.* **9**, 85 (1997).
5. J. H. Ferziger, Large eddy simulation, in *Simulation and Modeling of Turbulent Flows*, edited by T. B. Gatski, M. Y. Hussaini, and J. L. Lumley (Oxford Univ. Press, London 1996), pp. 109–154.
6. C. Fureby, G. Tabor, H. Weller, and D. Gosman, A comparative study of subgrid scale models in homogeneous isotropic turbulence, *Phys. Fluids* **9**, 1416 (1997).
7. A. Y. Kuo and S. Corrsin, Experiment on the geometry of the fine-structure regions in fully developed turbulent fluid, *J. Fluid Mech.* **56**, 447 (1971).
8. E. D. Siggia and G. S. Patterson, Intermittency effects in a numerical simulation of stationary three dimensional turbulence, *J. Fluid Mech.* **86**, 567 (1988).
9. J. Jimenez, A. Wray, P. Saffman, and R. Rogallo, The structure of intense vorticity in isotropic turbulence, *J. Fluid Mech.* **255**, 65 (1993).
10. A. Vincent and M. Meneguzzi, The spatial structure and statistical properties of homogeneous turbulence, *J. Fluid Mech.* **225**, 1 (1994).
11. D. H. Porter, A. Pouquet, and P. R. Woodward, Kolmogorov-like spectra in decaying three-dimensional supersonic flows, *Phys. Fluids* **6**, 2133 (1994).
12. J. Jimenez, Kinematic alignment effects in turbulent flows, *Phys. Fluids A* **4**, 652 (1992).
13. R. M. Kerr, Higher order derivative correlation and the alignment of small scale structures in numerical turbulence, *J. Fluid Mech.* **153**, 31 (1985).
14. W. T. Ashurst, A. R. Kerstein, R. M. Kerr, and C. H. Gibson, Alignment of vorticity of scalar gradients with strain rate in simulated Navier–Stokes turbulence, *Phys. Fluids* **30**, 2343 (1987).
15. D. I. Pullin and P. G. Saffman, Reynolds stresses and one-dimensional spectra for a vortex model of homogeneous anistropic turbulence, *Phys. Fluids* **6**, 1787 (1994).
16. A. Misra and D. I. Pullin, A vortex based subgrid stress model for large eddy simulation, *Phys. Fluids* **9**, 2443 (1997).
17. S. A. Orszag and I. Staroselsky, Computing, fluid dynamics, and all that, in *CFD99 Proceedings*, edited by J. Militzer (Dalhousie University, Halifax, Canada, 1999), p. 1.19.
18. J. Jimenez, private communication; see also *AIAA* 98-2891, 1998.
19. L. Shao, S. Sarkar, and C. Pantano, On the relationship between the mean flow and subgrid stresses in large eddy simulation of turbulent shear flows, *Phys. Fluids* **11**, 1229 (1999).
20. J. P. Boris and D. L. Book, Flux corrected transport I, SHASTA, a fluid transport algorithm that works, *J. Comput Phys.* **11**, 38 (1973).

21. P. Colella and P. R. Woodward, The piecewise parabolic method (PPM) for gas dynamic simulations, *J. Comput Phys.* **54**, 174 (1984).
22. J. P. Boris, F. F. Grinstein, E. S. Oran, and R. J. Kolbe, New insights into large eddy simulation, *Fluid Dyn. Res.* **10**, 199 (1992).
23. C. Fureby and F. F. Grinstein, Monotonically integrated large eddy simulation of free shear flows, *AIAA J.* **37**, 544 (1999).
24. P. L. Lions, *Mathematical Topics in Fluid Mechanics* (Oxford Sci., Oxford, 1996).
25. B. Vreman, B. Geurts, and H. Kuerten, Realizability conditions for the turbulent stress tensor in large eddy simulation, *J. Fluid Mech.* **278**, 351 (1994).
26. C. G. Speziale, Galilean invariance of subgrid scale stress models in the large eddy simulation of turbulence, *J. Fluid Mech.* **156**, 55 (1985).
27. G. F. Smith, On isotropic functions of symmetric tensors, skew symmetric tensors and vectors, *Int. J. Eng. Sci.* **9**, 899 (1971).
28. W. C. Reynolds, The potential and limitations of direct and large eddy simulations, in *Wither Turbulence? Turbulence at the Crossroads*, edited by J. L. Lumley, Lecture Notes in Physics (Springer-Verlag, Berlin/ New York, 1990), Vol. 357, p. 313.
29. J. S. Smagorinsky, General circulation experiments with primitive equations, *Mon. Weather Rev.* **94**, 99 (1963).
30. M. Germano, U. Piomelli, P. Moin, and W. H. Cabot, A dynamic subgrid scale eddy viscosity model, *Phys. Fluids A* **3**, 1760 (1994).
31. U. Schumann, Subgrid scale model for finite difference simulation of turbulent flows in plane channels and annuli, *J. Comput. Phys.* **18**, 376 (1975).
32. W. W. Kim and S. Menon, *A New Dynamic One Equation Subgrid Scale Model for Large Eddy Simulations*, AIAA Paper 95-0356 (1995).
33. T. Voelkl, D. I. Pullin, and D. C. Chan, A physical-space version of the stretched-vortex subgrid-stress model for large eddy simulation, *Phys. Fluids* **12**, 1810 (2000).
34. J. Bardina, J. H. Ferziger, and W. C. Reynolds, *Improved Subgrid Scale Models for Large Eddy Simulations*, AIAA Paper 80-1357 (1980).
35. S. Liu, C. Menevau, and J. Katz, On the properties of similarity sub-grid scale models as deduced from measurements in a turbulent jet, *J. Fluid Mech.* **275**, 83 (1994).
36. J. W. Deardorff, The use of subgrid transport equations in a three-dimensional model of atmospherical turbulence, *J. Fluids Eng. Trans ASME* **95**, 429 (1973).
37. R. A. Clark, J. H. Ferziger, and W. C. Reynolds, Evaluation of sub-grid scale models using an accurately simulated turbulent flow, *J. Fluid Mech.* **91**, 1 (1979).
38. C. Fureby, G. Tabor, H. G. Weller, and A. D. Gosman, On differential subgrid scale stress models in large eddy simulations, *Phys. Fluids* **9**, 3578 (1997).
39. C. A. J. Fletcher, *Computational Methods in Fluid Dynamics* (Springer-Verlag, Berlin/New York, 1992).
40. C. Hirsch, *Numerical Computation of Internal and External Flows* (Wiley, New York, 1999).
41. R. J. LeVeque, *Numerical Methods for Conservation Laws*, 2nd ed. (Birkhüser, Berlin, 1992).
42. S. K. Godunov, A difference method for numerical calculation of discontinuous solutions of the equations of hydrodynamics, *Mat. Sb.* **47**, 271 (1959).
43. V. Borue and S. A. Orszag, Local energy flux and subgrid-scale statistics in three dimensional turbulence, *J. Fluid Mech.* **366**, 1 (1998).
44. A. Harten, On a class of high resolution total variation stable finite difference schemes, *SIAM J. Numer. Anal.* **21**, 1 (1984).
45. F. F. Grinstein and C. Fureby, *Recent Progress on MILES for High Re Flows*, AIAA Paper 2002-0134 (2002); *J. Fluids Eng.,* 2002, in press.
46. P. L. Roe, Some contributions to the modelling of discontinuous flows, *Lect. Appl. Math.* **22**, 163 (1985).
47. H. Jasak, H. G. Weller, and A.D. Gosman, High resolution NVD differencing scheme for arbitrarily unstructured meshes, *Int. J. Numer. Meth. Fluids* **31**, 431 (1999).
48. G. Comte-Bellot and S. Corrsin, Simple Eulerian time correlations of full and narrow band velocity signals in grid generated 'isotropic' turbulence, *J. Fluid Mech.* **46**, 273 (1971).

49. F. F. Grinstein and C. R. DeVore, Dynamics of coherent structures and transition to turbulence in free square jets, *Phys. Fluids* **8**, 1237 (1996).
50. F. F. Grinstein, Self-induced vortex ring dynamics in subsonic rectangular jets, *Phys. Fluids* **7**, 2519 (1995).
51. J. P. Boris, J. Gardner, A. Landsberg, G. Patniak, and E. S. Oran, *LCPFCT—A Monotone Algorithm for Solving Continuity Equations*, NRL Memorandum Report 6410, Washington, DC (1993).
52. C. R. DeVore, *Flux-Corrected Transport Algorithms for Two-Dimensional Compressible Magnetohydrodynamics*, NRL Memorandum Report No. 6544, Washington, DC (1989).
53. F. F. Grinstein and R. H. Guirguis, Effective viscosity in the simulation of spatially evolving shear flows with monotonic FCT models, *J. Comput. Phys.* **101**, 165 (1992).
54. J. Jeong and F. Hussain, On the identification of a vortex, *J. Fluid Mech.* **285**, 69 (1995).
55. O. Andreassen, P. O. Hvidsten, D. C. Fritts, and S. Arendt, Vorticity dynamics in a breaking internal gravity wave. Part 1. Initial instability evolution, *J. Fluid Mech.* **367**, 27 (1998).
56. F. F. Grinstein, Vortex dynamics and entrainment in rectangular free jets, *J. Fluid Mech.* **437**, 69 (2001).
57. J. Zhou, R. J. Adrian, S. Balachandar, and T. M. Kendall, Mechanisms for generating coherent packets of hairpin vortices in channel flows, *J. Fluid Mech.* **378**, 353 (1999).
58. M. Kiya, K. Toyoda, H. Ishii, M. Kitamura, and T. Ohe, Numerical simulation and flow visualization experiment on deformation of pseudo-elliptic vortex rings, *Fluid Dyn. Res.* **10**, 117 (1992).
59. F. Hussain and H. S. Husain, Elliptic jets. Part I. Characteristics of unexcited and excited jets, *J. Fluid Mech.* **208**, 257 (1989).
60. S. G. Saddoughi, Local isotropy in high Reynolds number turbulent shear flows, in *CTR Annual Research Briefs* (Stanford Univ. Press, Stanford, CA, 1992), p. 237.
61. N. D. Sandham and R. J. A. Howard, *Statistics Databases from Direct Numerical Simulation of Fully-Developed Turbulent Channel Flow*, QMW-EP-1106 (Queen Mary & Westfield College, Department of Engineering, London, 1995).
62. R. A. Antonia, M. Teitel, J. Kim, and L .W. B. Browne, Low-Reynolds-number effects in a fully developed turbulent channel flow *J. Fluid Mech.* **236**, 579 (1992).
63. T. Wei and W. W. Willmarth, Reynolds number effects on the structure of a turbulent channel flow, *J. Fluid Mech.* **204**, 57 (1989).
64. R. B. Dean, Reynolds number dependence of skin friction and other bulk flow variables in two-dimensional rectangular duct flow, *Trans. ASME I J. Fluids Eng.* **100**, 215 (1978).
65. C. R. Smith and J. D. A. Walker, Turbulent wall-layer vortices, in *Fluid Vortices*, edited by S. Green (Kluwer Academic, Dordrecht/Norwell, MA, 1995), pp. 235–290.
66. R. F. Blackwelder, Boundary layer transition, *Phys. Fluids* **22**, 583 (1979).
67. J. Jeong, F. Hussain, W. Shoppa, and J. Kim, Coherent structures near the wall in a turbulent channel flow, *J. Fluid Mech.* **332**, 185 (1997).
68. P. Moin and J. Kim, Large eddy simulation of turbulent channel flow, *J. Fluid Mech.* **118**, 341 (1982).
69. G. Comte-Bellot, *Ecoulment Turbulent Entre deaux Parois Paralleles*, Publications Scientifiques et Techniques du Ministere de l'Air No. 419 (1965).
70. K. Tsuboi, T. Tamura, and K. Kuwahara, *Numerical Study of Vortex Induced Vibration of a Circular Cylinder in High Reynolds Number Flow*, AIAA Paper 89-1824 (1989).
71. E. Garnier, M. Mossi, P. Sagaut, P. Comte, and M. Deville, On the use of shock-capturing schemes for large eddy simulation, *J. Comput. Phys.* **153**, 273 (1999).
72. V. Sytine, D. H. Porter, P. R. Woodward, and S. W. Hodson, Convergence tests for the piecewise parabolic method and Navier–Stokes solutions for homogeneous compressible turbulence, *J. Comput. Phys.* **158**, 225 (2000).
73. N. Okong'o, D. D. Knight, and G. Zhou, Large eddy simulations using an unstructured grid compressible Navier–Stokes algorithm, *Int. J. Comp. Fluid Dyn.* **13**, 303 (2000).
74. G.-S. Karamanos and G. E. Karniadakis, A spectral vanishing viscosity method for large-eddy simulations, *J. Comput. Phys.* **163**, 22 (2000).